

EFFECT OF GLAZE VARIABLES ON THE MECHANICAL
STRENGTH OF WHITEWARES

BY

JENNIFER L. BENSON

A THESIS
SUBMITTED TO THE FACULTY OF

ALFRED UNIVERSITY

IN PARTIAL FULFILLMENT OF THE REQUIREMENTS
FOR THE DEGREE OF

MASTER OF SCIENCE

IN

CERAMIC ENGINEERING

ALFRED, NEW YORK

JULY, 2003

Alfred University theses are copyright protected and may be used for education or personal research only. Reproduction or distribution in part or whole is prohibited without written permission from the author.

EFFECT OF GLAZE VARIABLES ON THE MECHANICAL STRENGTH
OF WHITEWARES

BY

JENNIFER L. BENSON

B.S. ALFRED UNIVERSITY (2001)

SIGNATURE OF AUTHOR _____ (Signature on file)

APPROVED BY _____ (Signature on file)

JAMES R. VARNER, ADVISOR

_____ (Signature on file)

DAVID A. EARL, ADVISORY COMMITTEE

_____ (Signature on file)

WILLIAM M. CARTY, ADVISORY COMMITTEE

_____ (Signature on file)

PAUL F. JOHNSON, CHAIR, ORAL THESIS DEFENSE

ACCEPTED BY _____ (Signature on file)

ALASTAIR CORMACK, DEAN,
SCHOOL OF ENGINEERING

ACKNOWLEDGMENTS

I would like to thank sincerely thank Dr. James Varner for his assistance and guidance throughout this research. I would also like to extend a special thanks to Dr. William Carty for all of his help and knowledge on this topic. I would also like to thanks Dr. David Earl for counseling of various aspects of this investigation. Their help and support made many of difficult aspects of this research possible.

Great appreciation is extended to Gary Carnahan and Paul Pustulka of Lapp Insulators, Inc. for providing samples and allowing me to fire countless samples there. I would also like to thank Jeanette Harris for all of her technical assistance in the computer department.

Lastly, I would like to thank my family for all of their support throughout this seemingly endless stretch of schooling. I would also like to thank Aubree Buchtel and Rob Hausrath for their support during our extremely important meetings. Lastly, I would like to thank everyone else in Dr. Carty's research group for all of their help and support over the years.

TABLE OF CONTENTS

	Page
Acknowledgments.....	iii
Table of Contents.....	iv
List of Tables.....	vii
List of Figures	viii
Abstract.....	xii
1 INTRODUCTION.....	1
1.1 Literature Review.....	2
1.1.1 Coatings & Strength.....	2
1.1.2 Role of Glaze Oxides	6
1.1.3 Glaze/Body Interactions.....	7
1.1.4 Fractography of Whitewares	7
1.1.4.1 Mist/Velocity Hackle, Mirrors, and Fracture Origins.....	8
1.1.4.2 Wallner Lines.....	9
1.1.4.3 Hackle.....	9
1.1.4.4 Previous Fractography Findings of Glazed Whitewares ...	9
1.1.4.5 Fracture Mechanics	10
1.1.4.6 Weibull Statistics	11
2 EXPERIMENTAL PROCEDURE.....	14
2.1 Initial Glaze Studies.....	14
2.1.1 Glaze Matrix.....	14
2.1.2 Pyrometric-Cone-Equivalent (PCE) Test	15
2.1.3 Measurement of Coefficient of Thermal Expansion (CTE).....	15
2.2 Sample Preparation.....	17
2.2.1 Sample Forming.....	17
2.2.2 Glaze Preparation	18
2.2.2.1 Glaze B Fired to 1350°C.....	20
2.2.3 Glaze Application	20
2.3 Strength Testing	20

2.3.1 Loading Rate.....	22
2.3.2 Four-Point Flexure	24
2.4 Measured Glaze Stress Levels.....	25
2.5 Property Measurements	26
2.5.1 Young’s Modulus and Poisson’s Ratio.....	26
2.5.2 Bulk Density Measurements	26
2.6 Fractography Analysis	27
2.6.1 Scanning Electron Microscope (SEM) Analysis	27
2.7 X-Ray Diffraction (XRD)	27
2.7.1 Qualitative XRD	27
2.7.2 Quantitative XRD	27
2.7.2.1 Sample Preparation.....	28
2.7.2.2 Profile Fitting.....	28
2.7.2.3 Percent Quartz Calculation.....	29
3 RESULTS AND DISCUSSION	30
3.1 Determination of Coefficient of Thermal Expansion Values.....	30
3.2 CTE as a Function of Composition.....	31
3.2.1 Qualitative XRD Analysis	34
3.2.2 Quantitative XRD Analysis	37
3.3 Strength Testing	38
3.3.1 Effect of Glaze Composition.....	38
3.3.1.1 Silica Body.....	38
3.3.1.2 Alumina Body	40
3.3.1.3 Effect of CTE Mismatch on Normalized Strength	42
3.4 Effect of Glaze Thickness.....	44
3.5 Stress Calculations.....	47
3.5.1 Theoretical Stress Levels.....	47
3.5.2 Measured Glaze Stress Levels	51
3.6 Fracture Analysis.....	54
3.6.1 Comparison of Fracture Surfaces of the Bodies	54
3.6.2 Comparison of Glaze Thickness for Each Body.....	56
3.6.3 Weibull Analysis.....	59

3.7 Glaze/Body Interface	65
4 CONCLUSIONS	67
5 FUTURE WORK.....	69
REFERENCES	70
APPENDIX A	74
APPENDIX B	75
APPENDIX C	77
APPENDIX D	78
APPENDIX E	79

LIST OF TABLES

	Page
Table 1-I. Role of Various Glaze Oxides.....	6
Table 2-I. Glaze Matrix Used for Final Glaze Compositions	15
Table 2-II. Raw Materials of Bodies.....	18
Table 2-III. Raw Materials of Glazes A and B (endpoint glazes).....	18
Table 2-IV. Blend of Intermediate Glaze Compositions	19
Table 2-V. Glaze Compositions as Unity Molecular Formulae.....	19
Table 2-VI. Average Strength Values for Unglazed Bodies	23
Table 2-VII. Property Values of Glazes and Bodies.....	26
Table 2-VIII. 2 θ Ranges for Quantitative XRD Analysis.....	28
Table 3-I. CTE, T _g , and T _s Values of Glazes and Bodies.....	32
Table 3-II. Strength Difference Caused by Glaze Thickness	44
Table 3-III. Theoretical Stress Values of the Specimens	49
Table 3-IV. Fracture Origin Characterization for Silica-Body Samples	60
Table 3-V. Fracture Origin Characterization of Alumina-Body Samples	61
Table 3-VI. σ , m, and R ² Values for the Silica Body Samples	64
Table 3-VII. σ , m, and R ² Values for Alumina Body Samples	64

LIST OF FIGURES

	Page
Figure 1.1. A schematic of a glaze/body system.	3
Figure 1.2. An electrical porcelain with a distinct mirror and mist/velocity hackle surrounding it.	8
Figure 2.1. Method of tangents used to determine T_g and T_s	17
Figure 2.2. New fixture that was built for strength testing.	21
Figure 2.3. Schematic of the new fixture, with an enlargement of the cradle scheme.	21
Figure 2.4. The effect of loading rate on the mechanical strength of the alumina body and silica body.	23
Figure 2.5. Schematic of four-point flexure test.	25
Figure 2.6. Schematic of a "warp test" sample after firing.	25
Figure 2.7. Quantitative XRD internal standard calibration curve for quartz 29	29
Figure 3.1. Effect of $\text{SiO}_2/\text{Al}_2\text{O}_3$ ratio and the amount of SiO_2 on the CTE of the glaze.	32
Figure 3.2. CTE curves for Glasses A, B, C, D and the bodies.	33
Figure 3.3. CTE curves for Glasses E, F, Base, and B(1350) and the bodies... 34	34
Figure 3.4. XRD pattern of Glaze B and Glaze B fired to 1350°C..... 35	35
Figure 3.5. XRD pattern of Glaze F.	36
Figure 3.6. XRD pattern of Glaze B applied to the alumina and silica bodies.... 37	37
Figure 3.7. XRD pattern of Glaze B and Glaze B fired to 1350°C with fluorite added.	38

Figure 3.8.	The effect of thermal expansion mismatch between the body and glaze on measured strength for the silica body.....	39
Figure 3.9.	SEM micrograph of an alumina-body sample, glazed with glaze B(1350)	41
Figure 3.10.	The effect of thermal expansion mismatch between the body and glaze on the measured strength of the alumina body.....	41
Figure 3.11.	The effect of thermal expansion mismatch between the body and glaze when the measured strength has been normalized to the Young's Modulus of the silica body.	43
Figure 3.12.	The effect of thermal expansion mismatch between the body and glaze when the measured strength has been normalized to the Young's Modulus of the alumina body.....	43
Figure 3.13.	SEM photomicrograph of crystal growth seen on the glaze surface of Glaze A, twice-dipped on the alumina body	45
Figure 3.14.	SEM micrograph of the glaze surface of Glaze A, once-dipped, on the alumina body.	45
Figure 3.15.	SEM photomicrograph of crystal growth found on the glaze surface of Glaze D, twice-dipped, on the alumina body	46
Figure 3.16.	SEM photomicrograph of the glaze surface of Glaze D, once-dipped, on the alumina body	47
Figure 3.17.	Theoretical stress levels present in the glaze based on the thermal expansion mismatch between the glaze and the silica body.	50
Figure 3.18.	Theoretical stress levels present in the glaze based on the thermal expansion mismatch between the glaze and the alumina body.....	50
Figure 3.19.	Calculated residual glaze stress levels, for the silica-body samples, determined using the "warp test" method.	52
Figure 3.20.	Calculated residual glaze stress levels, for the alumina-body samples, determined from the "warp test" method.....	52

Figure 3.21. Image of "warp test" silica body samples after firing.....	53
Figure 3.22. Image of "warp test" alumina body samples after firing.	53
Figure 3.23. Low-magnification optical image of a typical low-strength silica sample, dipped with Glaze A.....	54
Figure 3.24. A low-magnification optical image of a high-strength silica sample, dipped with the Base glaze.....	55
Figure 3.25. A low-magnification SEM image of a typical fracture surface of a low-strength alumina sample, dipped with Glaze B.....	55
Figure 3.26. A low-magnification optical image of a typical fracture surface of a high-strength alumina body sample, dipped with the Base glaze.	56
Figure 3.27. SEM photomicrograph of a typical fracture origin for alumina-body specimens with the Base glaze, once-dipped.....	57
Figure 3.28. Low-magnification optical micrograph and a high-magnification SEM micrograph of a typical fracture origin for alumina-body specimens with the Base glaze, twice-dipped.....	57
Figure 3.29. SEM micrograph of a typical fracture origin for alumina-body specimens with Glaze E, once-dipped.	58
Figure 3.30. SEM micrograph of a typical fracture origin for alumina-body specimens with Glaze E, twice-dipped.....	58
Figure 3.31. SEM micrograph of a pore at the glaze/body interface as the strength-limiting flaw for alumina-body specimens with Glaze C, once-dipped.	59
Figure 3.32. SEM micrograph of a bubble in the glaze as the strength-limiting flaw for alumina-body specimens with Glaze C, twice-dipped.	59
Figure 3.33. Weibull plot for the silica body, for the once-dipped samples.	62
Figure 3.34. Weibull plot for the silica body, twice-dipped samples.....	62

Figure 3.35. Weibull plot for the alumina body, once-dipped samples.....	63
Figure 3.36. Weibull plot for the alumina body, twice-dipped samples.	63
Figure 3.37. SEM micrograph of a high-strength sample, Base glaze on the silica body, with a nondistinct glaze/body interface.....	65
Figure 3.38. SEM micrograph of a low-strength sample, Glaze D on the alumina body, with a distinct glaze/body interface.	66

ABSTRACT

Glaze thickness and glaze composition were systematically altered to study their effects on the mechanical strength of two commercial porcelain bodies, an alumina body and a silica body. This study determined that glaze composition affects the mechanical strength of porcelain piece in a linear fashion. The mechanical strength of a porcelain piece can then be predicted, accounting for the Young's Modulus of the body.

Maximum strengths values were achieved for the silica body at a thermal expansion mismatch level, between the body and glaze, of $0.93 \times 10^{-6}/K$. This corresponded to a mechanical strength of 97 MPa. It was not determined if a maximum had been reached for the alumina body, because when the amount of thermal expansion mismatch was the greatest, a surface layer was present on the body that caused large voids at the glaze/body interface during application of the glaze.

Fractography analysis was used to identify, when possible, fracture origins. This analysis attempts to correlate fracture origin sizes with strength, and the variation in fracture origin size to the scatter in the strength data. Fracture origins were, generally, identified as bubbles in the glaze for the lowest-strength samples, grains and pores at the glaze/body interface for the intermediate-strength samples, and grains and inclusion in the body for the highest-strength samples.

1 INTRODUCTION

The mechanical strength of a whiteware piece is crucial to manufacturers and customers alike. A significant amount of work has been done to evaluate the effects of several glaze variables on the strength of a piece.¹⁻⁸ However, little has been done to determine the strength-limiting flaws of fractured pieces. It has always been assumed that strength-limiting flaws could be attributed to inhomogeneities in a glaze or cracking of or around quartz particles. Recent work done by Pinto disputes this last issue. His results indicate that in fact the critical flaw size is actually three to four times larger than the quartz particle size.⁹ Little work has been done to try to correlate the effects of glaze variables with the location of strength-limiting flaws. It was the goal of this work to determine what effect glaze variables have on mechanical strength of commercial quartz and alumina porcelain bodies and to locate and identify the strength-limiting flaws.

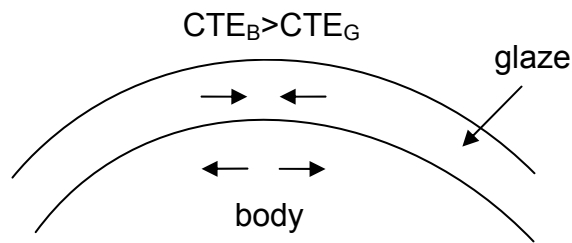
The application of a glaze to increase the strength of a piece is often oversimplified. Many factors must be taken into account. The present work looked at the effects of glaze thickness and thermal expansion mismatch between the body and glaze, through systematic alterations of the amount of silica in the glaze, on the mechanical strength of commercial porcelain bodies. Strength tests were performed, strength-limiting flaws were located and identified when possible, and statistical analysis was performed on the data.

Fractography analysis was conducted on selected specimens within each set. The strength-limiting flaws were located (when possible). Fracture mechanics was used in the fractographic analysis to verify that the correct feature was identified as the fracture origin. Weibull statistics were performed on the strength data to determine the distributions of strengths for each set of samples. Fractography was used in conjunction with Weibull statistics to confirm that only one type of flaw was the source of failure.

1.1 Literature Review

1.1.1 Coatings & Strength

It is observed that the application of a glaze, in a state of compression, to a whiteware piece will increase the mechanical strength of that piece.^{1-4,6,8} A glaze will be in a state of compression if it has a lower coefficient of thermal expansion than the body. Figure 1.1 is a cartoon of this situation. As a glazed whiteware piece is cooling after it has been fired, stresses build up in the glaze and body due to the thermal expansion mismatch between the two. The body wants to contract more than the glaze, which causes the glaze to be placed in compression and the body in tension.⁶ This should cause an increase in strength because of the fact that ceramics break when placed in tension.⁴ If the glaze is placed in too much compression, however, shivering can occur. Shivering is when a sliver of glaze with body flakes off the piece, because the body has fractured. When a glaze is placed in a state of tension, i.e., when the glaze has a higher coefficient of thermal expansion than the body, a result called crazing can occur. Crazing occurs because the glaze wants to contract more than the body during cooling; it is therefore placed in tension, causing cracks, crazing, in the glaze. Crazing shows up as a network of hairline cracks in the glaze.^{10,11} A phenomenon known as delayed crazing can also occur due to “moisture expansion” of the body or an “after-contraction” of the glaze. If either the body or glaze is placed in a substantial amount of tension, failure will occur. This amount is dependent on the composition of the body and glaze.¹¹



$CTE_B < CTE_G$ - Glaze in tension
 -crazing occurs
 $CTE_B > CTE_G$ - Glaze in compression
 -this condition is ideal, but there is an optimal level
 -if the difference between the two is too great, shivering will occur

Figure 1.1 A schematic of a glaze/body system.

Early work done by Gerold,⁸ investigated the effect of glazes on the tensile and transverse strength of porcelains. He made the conclusion that a glaze was deemed satisfactory if it increased the strength of the porcelain. The mechanical strength of the porcelain dropped drastically when a poor fit glaze was applied.

Funk¹ showed that the amount of compressive stress on the surface was not as important as the smooth surface that the glaze provides for the improvement of strength of a body with a poor microstructure. This work showed that there was an increase in strength when a glaze, with the same thermal expansion as the body, was applied to the body. Strength was also, slightly increased as the thermal expansion mismatch was increased.

Funk, et al.² showed that there are several mechanisms for strength improvement by the glaze: (1) covering the body's surface flaws, (2) chemical interaction with the body constituents to promote crystal growth at the interface, (3) acting as a flux on the quartz grains, and (4) the glaze being in compression.

Work done by Lampron,³ showed that glazed samples had higher strength values than unglazed samples, even though some glazes were actually in tension. Funk, et al.² attribute this to the fact that the glaze covered surface flaws which were, therefore, not exposed to water in the atmosphere, thus eliminating slow crack growth due to stress corrosion.

Duke, et al.⁴ showed that strength increased two to four times when a compressive glaze was applied to a body, compared to the unglazed body. They, also, did not encounter any shivering as a result of a large thermal expansion mismatch between the body and glaze, but were limited by the refractoriness of the glaze.

In work done by Bell and Koenig,⁶ they showed that strength was increased by the application of a glaze in most cases. In no case was a significant decrease in strength noted. In only one case was a slight decrease in strength seen, and this was attributed to the fact that the glaze was in very little compression. The amount of glaze compression directly correlated to strength, as the amount of glaze compression was increased the strength also increased.

Thiess⁵ reported that glazes high in fluxes (feldspar and whiting) caused a considerable decrease in strength, while glazes high in clay and flint content showed an increase in strength over the unglazed body.

Feinberg⁷ varied the amount of CaO in the glaze in order to change the thermal expansion of the glaze, and, therefore, different levels of glaze compression. No correlation could be made though between the amount of glaze compression and the strength of the samples.

An early, but still useful approach for understanding the strength of brittle materials, such as porcelain, is the work of Griffith. In the Griffith approach, the overall strength of a brittle material like porcelain is determined by its elastic

modulus, fracture energy, and flaw size. Griffith developed his equation for circular internal cracks; therefore, the flaw size is the radius or the semi-length of internal flaws. When the Griffith's equation is used for surface cracks, the flaw size is the depth (or radius) of the surface crack, therefore, cracks at the surface only need to be half as large as internal cracks to have the same strength.¹² When porcelains are glazed, a flaw that was a surface flaw now becomes an internal flaw. This suggests the flaws on the porcelain surface are at least twice as great as those on the glaze surface. If it is assumed that flaws on the porcelain surface cause fracture for both glazed and unglazed specimens it will take ~40% more stress to propagate the flaw in the glazed specimen, due to the fact that the flaw has now become an internal flaw as opposed to a surface flaw.

The amount of stress in the body and glaze can be determined theoretically or experimentally. Theoretical values can be calculated using Young's modulus and Poisson's ratio of the body, the change in temperature (usually from room temperature to the set point (T_g) of the glaze), and the difference in thermal expansion between the glaze and body.¹³ Inaccuracies in theoretical calculations can occur, because it is difficult to consistently and accurately measure the thermal expansions of the body and glaze. This method also does not show all of the thermophysical characteristics of the glaze and body, including changes in viscosity and rigidity.^{6,14} Glaze stress levels can be determined experimentally by a few different methods. One method is the ring test. This consists of glazing the outside of a thin ring and firing the ring. Afterwards, the ring is slit with a saw, and the amount of deflection of the slit from its original position is measured. The amount of deflection of the slit is dependent on the amount of stress present in the glaze.¹⁵ Another method of determining glaze stress levels is by a test known as the "warp test." The amount of stress is measured by glazing one side of a bar and measuring the amount of deflection after firing. The residual stresses arising from the thermal expansion mismatch between the body and the glaze cause the system to bend.¹⁶

1.1.2 Role of Glaze Oxides

Only those oxides that were systematically varied in the glaze will be discussed. These include silica (SiO_2), alumina (Al_2O_3), calcium oxide (CaO), magnesium oxide (MgO), sodium oxide (Na_2O), and potassium oxide (K_2O). Table 1-I lists the various roles that each oxide has in the glass.

Table 1-I. Role of Various Glaze Oxides¹⁷

Oxide	Role
SiO_2	Principle glass-forming oxide, high melting temperature, high viscosity, high resistance to chemical attack, low thermal expansion, and increases hardness and strength
Al_2O_3	Refractory, very high viscosity, high resistance to chemical attack, increases strength and prevents devitrification
CaO	Principle flux in medium- and high-fire glazes, high resistance to chemical attack, low thermal expansion, and increases and strength
MgO	At low temperatures it is a matting agent and opacifier, at high temperatures it is a flux, high resistance to chemical attack, low thermal expansion, and increases strength
Na_2O	High thermal expansion, low melting temperature, low viscosity, low resistance to chemical attack, and lowers strength
K_2O	Similar to Na_2O but a slightly higher viscosity

The general rules for SiO_2 listed above can only be applied if it is assumed that there is no undissolved quartz present in the glaze. If undissolved quartz is present, the rule of increasing the SiO_2 level to decrease the thermal expansion is not valid. The thermal expansion of the glaze will actually increase significantly in the presence of undissolved quartz particles. The thermal expansion of the crystalline quartz particles is much greater than that of SiO_2 in the glassy phase.¹⁰

1.1.3 Glaze/Body Interactions

Reactions that take place at the glaze/body interface can have a significant impact on the mechanical strength of a whiteware piece. Parmelee¹⁸ states that interaction of the glaze and body depends on:

1. The nature and condition of the body
2. The glaze composition
3. Whether the glaze is fritted and to what extent
4. The temperature and duration of the firing
5. The glaze viscosity
6. The mutual solubility of body and glaze components

The reaction at the interface must be sufficient to hold the glaze to the body. The amount of glaze penetration also affects glaze fit. The amount of penetration can vary drastically and depends chiefly on the glaze composition and the character of the body.¹⁹ Duke et al.⁴ note that there is a strengthening effect due to increased interfacial reaction in glazed glass-ceramic systems. This effect has been attributed to strengthening of the system by the development of interlocking crystals at the interface. Work done by Feinburg,⁷ substantiates the claim that a glaze/body system with more crystalline growth has greater strength than systems with little growth. Cerdan and LaCourse²⁰ showed that a wide interface indicates a strong dissolution of the body by the glaze, i.e., a strong glaze/body interaction. Also, the glaze/body interface may be higher or lower in thermal expansion than either the glaze or the body due to localized variations, e.g., quartz grains at the interface.

1.1.4 Fractography of Whitewares

Fractography is useful for determining the cause of failure. To be able to understand how a sample failed it is important to understand various fracture markings that can be found on a fractured piece. This discussion will primarily be focused on fracture markings commonly found in whitewares.

Since whitewares are brittle materials, they fail in tension. Cracks therefore run perpendicular to the axis of local principal tension, and anything that disrupts this shifts the plane of the crack, and, therefore, marks the progress of the crack.²¹

1.1.4.1 Mist/Velocity Hackle, Mirrors, and Fracture Origins

Mist/velocity hackle is a fracture marking often found on whiteware fracture surfaces, particularly when failure was at high stress. Mist/velocity hackle is the rough surface of a fractured piece that shows the crack front ran through the region at terminal velocity (~ 1600 m/s).²¹ A region known as the mirror can be found inside the mist hackle (i.e., on the origin side). The fracture origin can commonly be found in the center of the relatively featureless mirror. The fracture origin is the flaw where the crack began. Fracture origins that are commonly found in whitewares include pores, cracks, agglomerates, and large particles. Locating the fracture origin is important, because this gives the most valuable information on why the piece failed. Figure 1.2 shows a commercial electrical porcelain with a distinct mirror and mist/velocity hackle that surrounds it.²¹

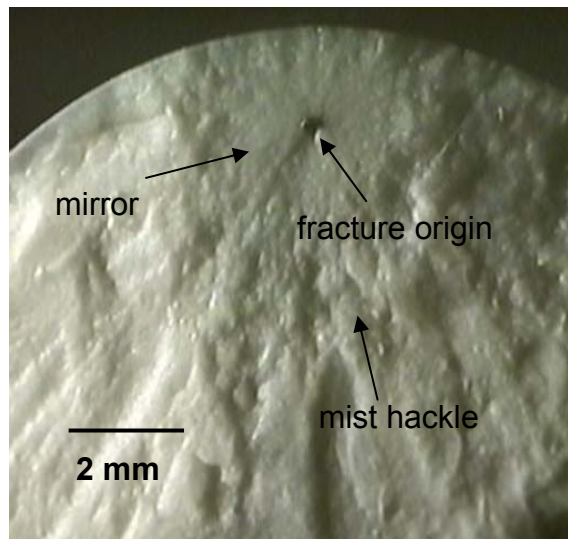


Figure 1.2 An electrical porcelain with a distinct mirror and mist/velocity hackle surrounding it. The fracture origin is located in the center of the mirror.

When characterizing fracture origins it is important to provide three pieces of information: (1) the type of flaw, e.g., pore or inclusion, (2) the location of the

flaw, e.g., bulk or surface, and (3) the size of the flaw, for circular flaws the diameter, and for any other geometry the major and minor axis should be stated.²²

1.1.4.2 Wallner Lines

Another important type of fracture markings are Wallner lines. These are easily distinguishable in glasses but are much difficult to see on whiteware fracture surfaces. Wallner lines in general can be described as the locus of intersection of a spreading elastic pulse with successive points along the running crack front. The concave side of the Wallner line is the side from which the crack came. Wallner lines are useful in determining the direction and velocity of cracking.^{21,23}

1.1.4.3 Hackle

There are several types of hackle which can be useful. Hackle can generally be described as elongated ridges on the fracture surface. Mist/velocity hackle was discussed previously. Wake hackle occurs when a crack encounters a discontinuity, e.g., an inclusion. When the crack front encounters the discontinuity it will divide and sweep past it on both sides. As the two fronts approach one another behind the discontinuity they generally do not meet, but proceed onward parallel to one another. The result is a single hackle step, trailing from the discontinuity in the direction of crack spread. Its name is derived from the resemblance to the wake seen downstream from a post in flowing water. Hackle is generally helpful in determining the direction of crack propagation.^{21,23}

1.1.4.4 Previous Fractography Findings of Glazed Whitewares

In work done by Lampron,³ fracture origins were primarily located at the glaze/body interface. When quartz grains >150 μm were observed, fracture started at the interface where the stress is the greatest. Work done by Funk et al.² also had fracture origins located at the glaze/body interface or in the body. Larger flaws were always found at the surface of the porcelain as opposed to the surface of the glaze; therefore, no origins were located in the glaze. Work done by Feinburg,⁷ also, had fracture origins located at the glaze/body interface or

slightly below this region. Funk¹ had origins that were located within the body, not at the glaze surface or the glaze/body interface.

1.1.4.5 Fracture Mechanics

Fracture mechanics should be used in conjunction with fractographic analysis to verify that the correct flaw has been identified as the flaw origin. The verification can be considered adequate if the calculated and fractographically measured flaw origin sizes agree within a factor of two or three. Certain requirements must be met in order to describe the relationship between strength and flaws: (1) the defects must be independent from each other, (2) the material must obey the “weakest-link hypothesis,” i.e., the largest defect causes failure of the entire piece, and (3) the critical defect density can be defined, and the size of the critical defects (c) correlates to the strength.^{24,25}

Flaw origin sizes can be estimated from fracture mirror sizes. It has been demonstrated and widely accepted that there is a relationship between fracture stress (σ) and the mirror radius (r_m) of a fractured surface. This relationship is stated as:

$$\sigma = Ar^{-\frac{1}{2}} \quad (1)$$

where A is a constant sometimes called the mirror constant. The inverse relationship between strength and the size of the mirror is due to the fact that when more stress is present at failure there is more stored energy present. The crack will then accelerate faster and reach maximum velocity in a shorter distance. Based on the theory of fracture mechanics, the fracture stress and critical flaw size (c) are related by:

$$c = \left(\frac{K_{IC}}{Y\sigma} \right)^2 \quad (2)$$

where K_{IC} is the critical stress intensity factor for a crack to propagate, and Y is a flaw geometry factor. Based on equations (1) and (2), the flaw size and the mirror size can be related as follows:

$$r = \left(\frac{Y^2 A^2 c}{K_{IC}^2} \right) \quad (3)$$

Since A and K_{IC} are constants for a given material, the ratio of flaw size to mirror size is a constant. For most glasses and polycrystalline ceramics, the ratio of the outer mirror ratio to flaw size is $\approx 13:1$. Materials will deviate from this value if interior pores rather than surface flaws generally are the source of failure or if severe microcracking takes place. Based on the equations above, it can be concluded that the mirror constant is proportional to the K_{IC} for glasses and polycrystalline ceramics.²⁵⁻²⁹

1.1.4.6 Weibull Statistics

Fracture stresses and statistical distribution of defects are closely connected to one another. Weibull statistics are the most commonly used form of statistics for characterizing the amount of scatter in the strength data of a sample set. The Weibull distribution is given by the equation

$$P_f = 1 - \exp \left(- \left(\frac{(\sigma - \sigma_t)^m}{\sigma_o} \right) \right) \quad (4)$$

where:

P_f =probability of failure

σ =stress at a point

σ_o =scale parameter

σ_t =threshold strength (σ_t is set to zero when using a two-parameter Weibull model)

m =Weibull modulus

Many assumptions must be made when using the Weibull model, including that (1) the material is homogeneous, (2) the defect population that limits strength is the same whatever shape or preparation method is used for tested specimens, (3) the defect populations are invariant with time, (4) the defects are randomly distributed and are small relative to the specimen size; there is a statistically significant number of defects within the specimen, and (5) only one failure mechanism is operative. The Weibull modulus is then determined, most commonly, by the least squares regression of the linearized form of Eq. 4. The probability of failure is calculated by $P_i=i/(N+1)$ where $i=1,2,3,\dots,N$.³⁰⁻³²

Industry uses Weibull statistics to determine the reliability of a product. The Weibull modulus is inversely related to the scatter within the strength data; i.e., a large Weibull modulus corresponds to low scatter in the data. However, even though the overall scatter in the data is important, it is the low-strength end of the distribution curve that is of particular interest, because these low strengths limit the design strength.³²

Fractography plays an important role when using Weibull statistics. As stated previously, only one type of fracture origin can be the cause of failure for Weibull statistics to be valid. This claim is either substantiated or refuted by the use of fractography. When there are multiple flaw populations, interpreting the results can become difficult. This topic is discussed later.

Doshi and Reed³³ showed that a wider distribution of flaw size, hence a smaller Weibull modulus, was caused by extensive machining damage. This is an important issue to companies that machine products in the green state. The machining could significantly reduce the reliability of the product. Doshi and Reed showed that the increase in Weibull modulus for other sets of samples, indicating a different flaw type and a narrower distribution of the flaw size, was due to different types of pores within the piece, and not machining damage.

Their investigation also showed that different sets of samples with the same Weibull moduli had similar flaw size distributions and critical flaw sizes.

As stated earlier, problems arise when there are multiple types of fracture origins. When two types of fracture origins are present, the Weibull distribution usually becomes bimodal. This case is actually the “norm and not the exception.”³⁰ However, a bimodal Weibull distribution is not proof that two types of fracture origins are present. Different flaw populations will have different strength distributions associated with them. A more complicated approach, by distinguishing how many pieces failed due to each flaw type, must be taken when trying to conduct Weibull statistics. This again reinforces the fact that fractography is an important part of the statistical process.^{30,31}

2 EXPERIMENTAL PROCEDURE

2.1 Initial Glaze Studies

2.1.1 Glaze Matrix

A sixteen-glaze matrix was created based on the unity molecular formula (UMF) approach first introduced by Seger.³⁴ The UMF approach is a simple way to address a matrix of glaze compositions. The matrix was selected based on the UMF of a base glaze (the UMF of the base glaze will be discussed in Section 2.2.2). Table 2-1 shows the matrix that was used. All other glaze compositions were systematically changed from that of the base glaze. The matrix is based on the ratio of molar equivalents of SiO_2 to Al_2O_3 , where the molar equivalents of Al_2O_3 was kept constant at approximately 0.43, and the molar equivalents of RO and R_2O used. The sum of RO and R_2O is always one (i.e., when 0.7 molar equivalents of RO are listed 0.3 molar equivalents of R_2O were also used). The final glaze compositions were selected from this matrix based on the results from the pyrometric-cone-equivalents tests. A list of the raw materials is located in Appendix A.

Table 2-I. Glaze Matrix Used for Final Glaze Compositions

Glaze Sample	SiO ₂ :Al ₂ O ₃	RO
1	6	0.7
2	6	0.8
3	6	0.9
4	6	1.0
5	8	0.7
6	8	0.8
7	8	0.9
8	8	1.0
9	10	0.7
10	10	0.8
11	10	0.9
12	10	1.0
13	12	0.7
14	12	0.8
15	12	0.9
16	12	1.0

2.1.2 Pyrometric-Cone-Equivalent (PCE) Test

The PCEs were created by adding corresponding amounts of each composition with ~10 wt% de-ionized water. Methyl cellulose (3% d.w.b.) was added to act as a binder. The plastic bodies were then formed into cones using a die supplied by Orton, Inc. (Westerville, OH). Each PCE was placed in a ring plaque with PCE standards and a PCE of the base glaze (PCE standards and ring plaques were also supplied by Orton, Inc., Westerville, OH). The PCEs were then fired in a box kiln, containing molydisilicide heating elements, (Alfred University, Alfred, NY) to a temperature of 1300 °C at 150 K/hr. The temperature at which each cone dropped was noted. Based on these results and the results of the dilatometry runs, the endpoint glaze compositions (A and B) were selected.

2.1.3 Measurement of Coefficient of Thermal Expansion (CTE)

CTE measurements were conducted on all glaze samples, initial glaze compositions, and glaze compositions used in later experiments, and each body composition. These measurements were done using a dilatometer (Orton Model

1600, Orton, Inc., Westerville, OH). A non-contact laser dilatometer (Experimental Model, Orton, Inc., Westerville, OH) was also used to verify the results. This type of dilatometer uses a laser to measure thermal expansion. The main advantage of this type of dilatometer is there is no sample deformation, at high temperatures, due to the force exerted on the sample by the push rod of the measuring system. Therefore, temperatures higher than the dilatometric softening point can be studied.³⁵ A bulk sample was made for each glaze composition. A sample ~3 cm in length was then cut from this using a low-speed saw. A sample of approximately the same length was cut for each body. The samples were heated in the dilatometer at a rate of 3 K/min. The glazes were heated until a -3.0% deformation occurred in the sample. The bodies were fired to a temperature of 1225°C. CTE values were determined for several temperature ranges, which include 200°C-500°C, 50°C- T_g , and 50°C- T_s (the importance of T_g and T_s will be discussed later).

T_g and T_s were determined by the method of tangents. Tangent lines were drawn on the curve of percent linear change versus temperature where sudden changes in slope occurred. Figure 2.1 shows an example of this method.

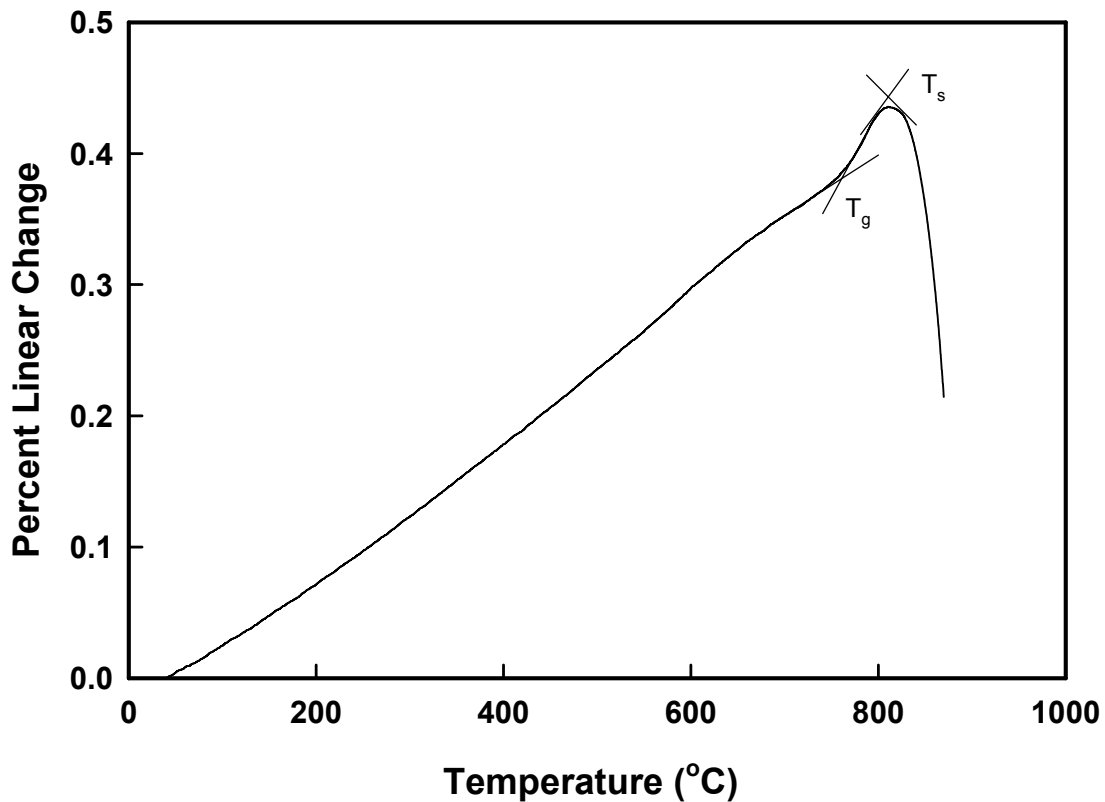


Figure 2.1. Method of tangents used to determine T_g and T_s .

2.2 Sample Preparation

2.2.1 Sample Forming

Two different body compositions were used. These bodies were obtained from Lapp Insulators, Inc. (LeRoy, NY). Table 2-II lists the raw materials used in the bodies. The plastic bodies had been made from a slurry that had been filter pressed and pug milled. The plastic bodies were then extruded into cylindrical rods, with dimensions of approximately 13 mm in diameter and 200 mm long. A vacuum of ~140 kPa was used to ensure all the air was removed during forming. These rods were then fired in an industrial tunnel kiln (Lapp Insulators, Inc., LeRoy, NY) using Lapp's 31-hour firing schedule that includes a 3-hour dwell at 1221°C.

Table 2-II. Raw Materials of Bodies

Raw Materials	Silica Body (% d.w.b.)	Alumina Body (% d.w.b.)
Clay	43.68	35.32
Feldspar	34.81	29.84
Flint	20.89	-
Bentonite	0.53	0.52
Alumina	-	34.32

2.2.2 Glaze Preparation

Seven different glaze compositions were used. The base glaze was supplied by Lapp Insulators, Inc. (LeRoy, NY). Two endpoint glazes (Glazes A and B) were selected based on the information supplied by the PCE tests and dilatometry testing. The endpoint compositions represented the largest and smallest coefficients of thermal expansion. Table 2-III lists the raw materials used to prepare Glazes A and B. The powders were milled overnight and then sieved through a 250µm sieve (sieve number 60). This was done to ensure that there were no agglomerates. 55-wt% suspensions were made and allowed to mix for an hour to ensure homogeneity.

Table 2-III. Raw Materials of Glazes A and B (endpoint glazes)

Raw Materials	Glaze A (% d.w.b.)	Glaze B (% d.w.b.)
G-200	50.79	36.90
EPK	9.44	8.66
Talc	9.33	6.67
CaCO ₃	14.26	10.34
Flint	14.99	36.46
Na-ash	0.29	0.21
K-ash	0.90	0.65

Glazes C, D, E, and F were blends of the Base glaze and Glaze A, and the Base glaze and Glaze B, respectively. Table 2-IV shows the blends used.

Table 2-IV. Blend of Intermediate Glaze Compositions

Glaze	Base (wt %)	A (wt %)	B (wt %)
C	66	33	-
D	33	66	-
E	66	-	33
F	33	-	66

Table 2-V lists the UMF of the glazes. All UMFs were calculated based on chemical analysis (ACME Analytical Labs LTD., Vancouver, BC) of the sample. Chemical analysis was done using ICP-AES (inductively couple plasma-atomic emission spectroscopy) using lithium borate digestion of the samples. Chemical analysis information is listed in Appendix A. A sample UMF calculation is shown in Appendix B.

Table 2-V. Glaze Compositions as Unity Molecular Formulae

Oxide	A	B	D	C	E	F	Base
Na ₂ O	0.08	0.09	0.07	0.06	0.06	0.07	0.03
K ₂ O	0.21	0.23	0.18	0.15	0.14	0.17	0.09
MgO	0.23	0.25	0.21	0.20	0.20	0.21	0.20
CaO	0.48	0.44	0.52	0.55	0.56	0.52	0.61
SrO	0.00	0.00	0.02	0.04	0.05	0.02	0.07
Al ₂ O ₃	0.43	0.46	0.42	0.41	0.42	0.42	0.42
ZrO ₂	0.00	0.00	0.06	0.16	0.18	0.08	0.31
SiO ₂	3.37	5.34	3.18	3.50	4.18	4.50	4.31

2.2.2.1 Glaze B Fired to 1350°C

This particular glaze was prepared as a frit. It had the same chemical composition as Glaze B, but was fired to a temperature of 1350°C, with a dwell time of 1 hour. The glass was then quenched in air. The glass was then crushed and ground using a mortar and pestle. A 50wt% suspension was prepared and ball milled for 12 hours to reduce the particle size of the frit. An organic suspending agent (3% d.w.b.) was added to reduce the amount of particle settling.

2.2.3 Glaze Application

All glazes were applied to unfired rods by dipping. The glaze was first placed in a graduated cylinder. The rods were then dipped into the glaze, leaving an end uncoated. To obtain a glaze thickness that was twice as thick as the original, the rods were dipped once, allowed to sit for ~30 seconds, and then dipped again. All glazed rods were allowed to dry for a minimum of 24 hours. The rods were then fired vertically, in refractory bricks with holes drilled in them, in the same industrial tunnel kiln (Lapp Insulators, Inc., LeRoy, NY) as the unglazed rods using the same firing schedule.

2.3 Strength Testing

Strength testing was carried out on a flexure testing device (Instron Model 8562, Instron Corp., Canton, MA). The ASTM C1161-94 standard procedure³⁶ was used, though the loading rate was varied for the testing of the unglazed samples to check the accuracy of the test. A new fixture was made based on the design by Quinn, Ives, Jahanmir, and Koshy.³⁷ Four cradles are at the distribution points. The cradles distribute the load evenly onto the test piece. This avoids severe contact stresses or wedging stresses. The loading rollers are free to roll to eliminate frictional constraints.³⁷ Figure 2.2 shows the new fixture that was used, while Figure 2.3 is a schematic of the fixture with an enlargement of the cradle scheme.

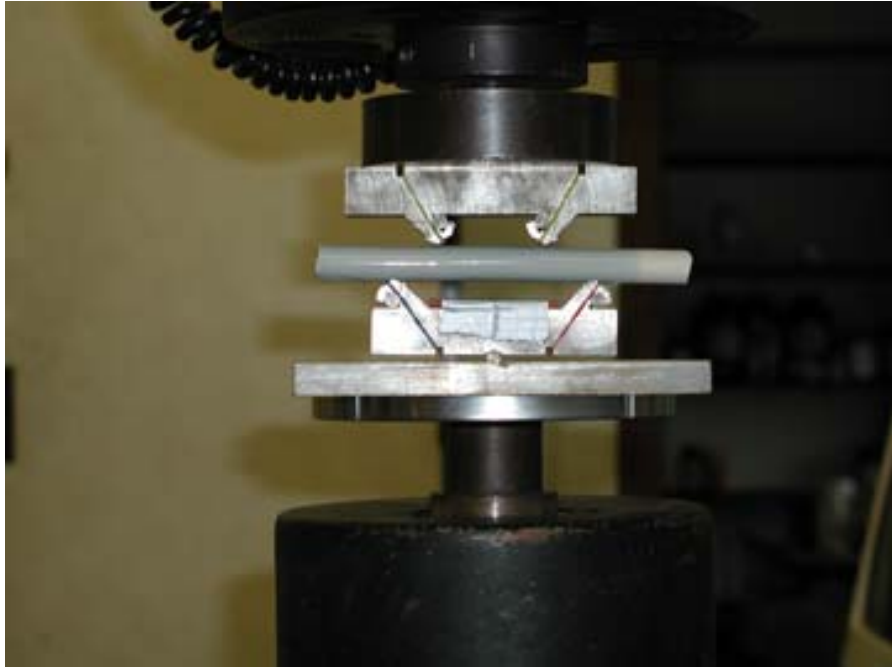


Figure 2.2. New fixture that was built for strength testing.

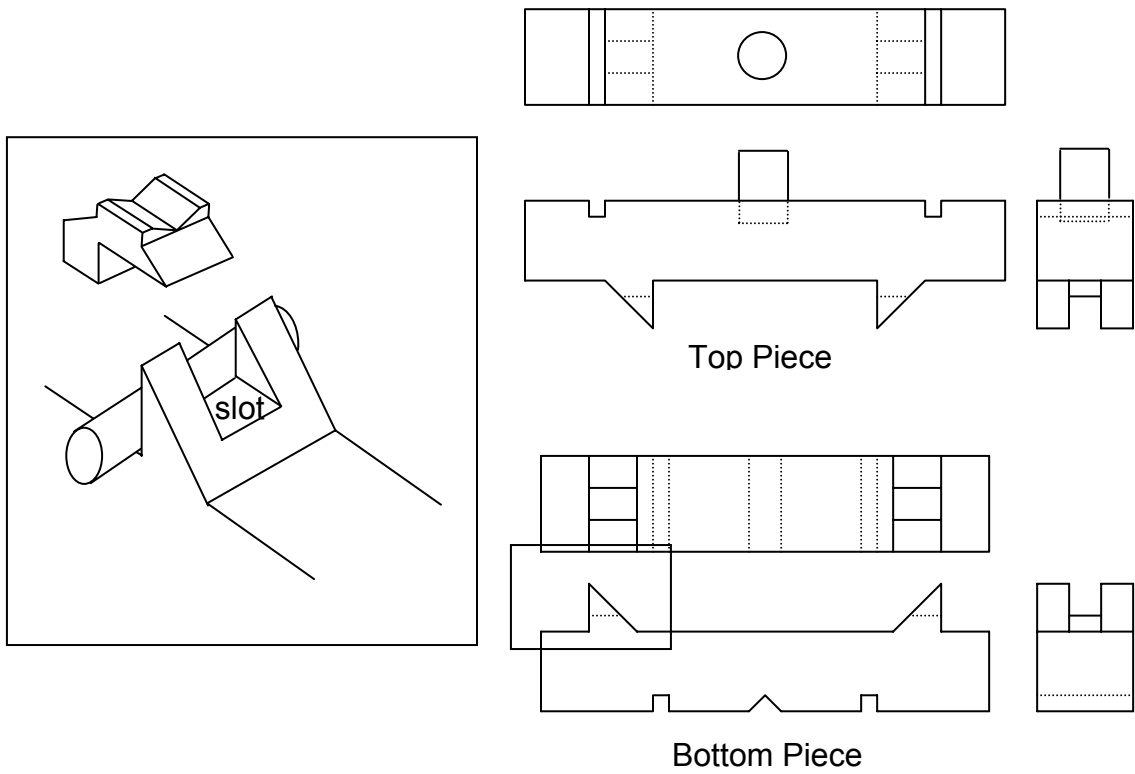


Figure 2.3. Schematic of the new fixture, with an enlargement of the cradle scheme.

2.3.1 Loading Rate

A study was conducted to determine the effect of loading rate on strength. 25 unglazed samples of each body were tested. The silica samples were tested using 0.05, 0.5, and 5.0 mm/min crosshead loading rates. The alumina samples were only tested using crosshead loading rates of 0.5 and 5.0 mm/min, due to the extremely long times of testing using the slowest rate.

Figure 2.4 the loading-rate test results for both the alumina and silica bodies. The error bars are two standard deviations. Table 2-VI lists the average strength values, \pm one standard deviation, for both bodies. For the alumina body, loading rate had no statistical effect on strength. This was determined with 95% confidence, using the analysis of variance. The standard deviation ranged from 6.5-8% for the alumina body. Loading rate did have a statistical effect on the strength of the silica body. The strength at the loading rate of 0.05 mm/min was statistically lower than the strengths at 0.5 and 5.0 mm/min. Loading rates of 0.5 and 5.0 mm/min showed no statistical difference in strength, with standard deviations ranging from approximately 3.5-5% for the silica body.

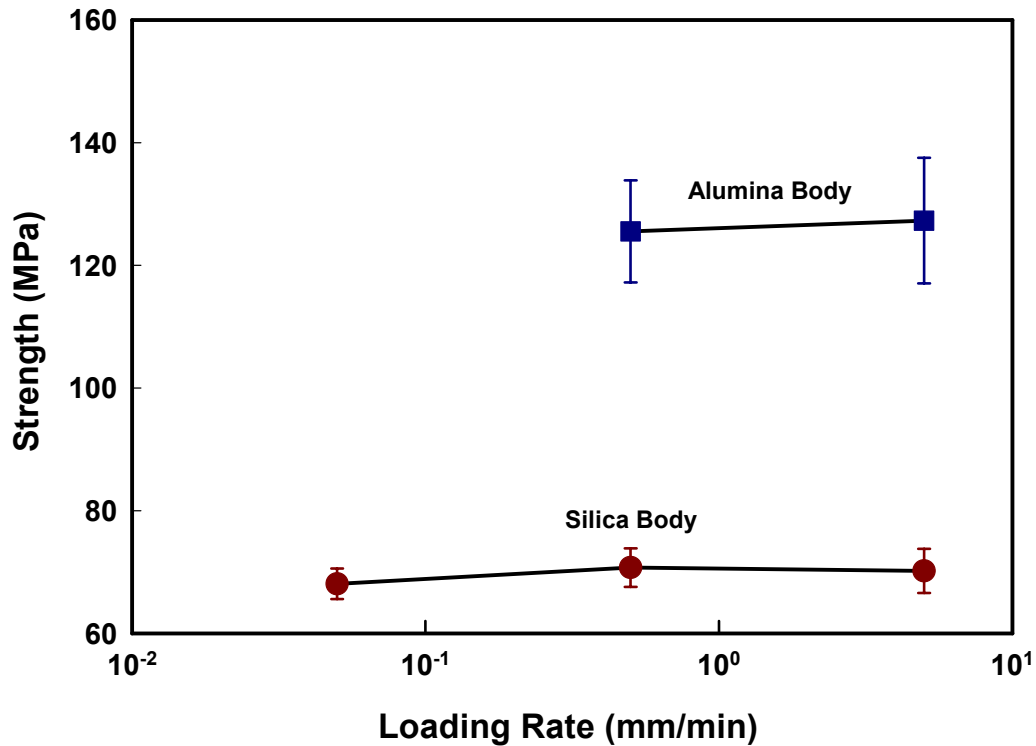


Figure 2.4. The effect of loading rate on the mechanical strength of the alumina body and silica body.

Table 2-VI. Average Strength Values for Unglazed Bodies

Loading Rate (mm/min)	Strength (MPa)	
	Silica Body	Alumina Body
0.05	68 ± 3	-
0.50	71 ± 3	126 ± 8
5.00	70 ± 4	127 ± 10

Slower loading rates often give lower strength values, in ceramics with a glassy phase, because stress-assisted corrosion, mainly of the glass at the crack tip, takes place when water is present. Slower loading rates provide more time for stress-assisted corrosion of the surface crack. Unglazed samples commonly have flaws that are exposed to the atmosphere; therefore, stress corrosion phenomena may occur. Since neither the alumina nor silica bodies showed a

statistical difference in strength between 0.5 and 5.0 mm/min loading rates, this suggests that strength is unaffected by stress corrosion above a certain minimum loading rate. This study verified that the ASTM standard loading rate of 5.0 mm/min was appropriate for strength testing.

2.3.2 Four-Point Flexure

25 rods from each sample were tested using a four-point flexure apparatus. All glazed samples were tested using a loading rate of 5.0 mm/min, as specified by ASTM C1161-94.³⁶ The loading fixture had an outer span of 80 mm and an inner span of 40 mm. Figure 2.5 is a schematic representation of flexure testing. It should be noted that all samples failed within the inner span, which is an indication that the fixture functioned correctly. All rods were tested to failure. The maximum load at failure was recorded for each sample. This value, along with sample and fixture dimensions, can be input into the formula for the strength of a beam in four-point flexure:

$$\sigma = \left(\frac{16Px}{\pi d^3} \right) (g) \quad (5)$$

where:

σ =strength (Pa)

P=load at failure (kgf)

x=(outer span-inner span)/2 (m)

d=diameter of specimen (m)

g=acceleration due to gravity (m/s²)

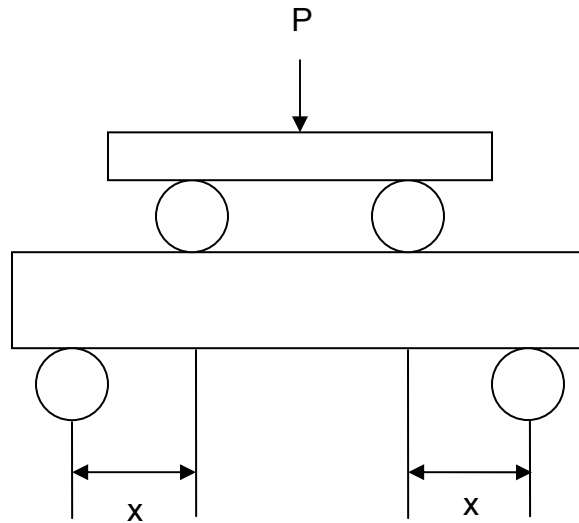


Figure 2.5. Schematic of four-point flexure test.

2.4 Measured Glaze Stress Levels

A technique known as a “warp test” was conducted to determine the amount of residual stress in the glaze caused by the differential thermal contraction of the glaze and substrate. The “warp test” was done by glazing one side of a bar substrate (50 x 12.5 x 2mm). A schematic of a sample after firing is shown in Figure 2.6. Two specimens for each glaze composition, glaze thickness, and body-composition combination were tested. The samples were fired at Lapp Insulator using the firing schedule as stated earlier. The amount of deflection of the bar after firing was measured.

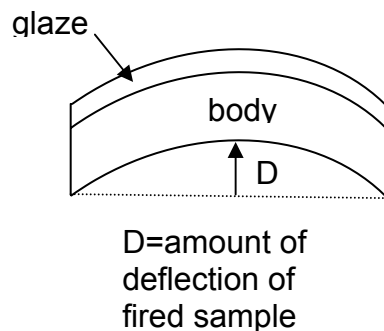


Figure 2.6. Schematic of a “warp test” sample after firing.

2.5 Property Measurements

2.5.1 Young's Modulus and Poisson's Ratio

Young's modulus and Poisson's ratio were determined using the pulse echo technique. This technique uses sound velocity through the material to calculate Young's modulus and Poisson's ratio. Five samples of each body and glaze were tested. The average value for each set was used in the stress calculations. The average Young's modulus and Poisson's ratio value for each set can be found in Table 2-VII. Example calculations of how Young's modulus and Poisson's ratio were determined can be found in the Appendix C.

2.5.2 Bulk Density Measurements

The bulk density of both bodies was measured using the ASTM C20-87 standard procedure.³⁸ Five samples of each body were measured, and the average bulk density value was used in the calculations for Young's modulus. The bulk densities of the glazes were measured using ASTM C693-93 standard procedure for determining the density of a glass.³⁹ Five samples of each glaze were tested. The average bulk density values, \pm one standard deviation, can be found in Table 2-VII.

Table 2-VII. Property Values of Glazes and Bodies

Sample	Density (g/cm ³)	Poisson's Ratio	Young's Modulus (GPa)
A	2.21 \pm 0.01	0.23 \pm 0.01	69 \pm 1
B	2.21 \pm 0.01	0.22 \pm 0.01	66 \pm 2
C	2.34 \pm 0.01	0.24 \pm 0.01	73 \pm 1
D	2.23 \pm 0.01	0.25 \pm 0.01	66 \pm 1
E	2.31 \pm 0.01	0.23 \pm 0.01	73 \pm 2
F	2.24 \pm 0.01	0.22 \pm 0.01	69 \pm 2
Base	2.51 \pm 0.01	0.23 \pm 0.02	82 \pm 2
Silica Body	2.47 \pm 0.01	0.19 \pm 0.03	83 \pm 3
Alumina Body	2.79 \pm 0.01	0.22 \pm 0.01	122 \pm 3

2.6 Fractography Analysis

Fractography analysis was done on a selected number of samples from each set. Two high-strength, two medium-strength and two low-strength samples were selected from each set. The samples were then observed under a low-magnification optical microscope to locate fracture origins. The samples were then examined using the SEM to identify (when possible) the location of the fracture origins and to study the glaze/body interface.

2.6.1 Scanning Electron Microscope (SEM) Analysis

The samples were mounted using carbon paste then were sputter coated with a conductive surface (60% Au and 40% Pd). Fracture origins were identified (when possible) using the SEM (AMRAY 1810). The glaze/body interface was also studied. Qualitative analysis was conducted on Glaze A samples using the SEM analytical accessory Energy-Dispersive X-Ray Spectrometer (EDS).

2.7 X-Ray Diffraction (XRD)

2.7.1 Qualitative XRD

XRD (Siemens D500 Goniometer, $\text{CuK}\alpha$ radiation, Alfred University, Alfred, NY) was used to determine if any undissolved quartz particles were present in the glaze. The samples tested were bulk fired glazes. The scan parameters used were 2θ range of $15\text{-}60^\circ$, step size of 0.03° , and a dwell time of 3 seconds. Phase identification was conducted using commercial software routines (Jade+, Version 6.0, Materials Data, Inc., Livermore, CA, 2002).

2.7.2 Quantitative XRD

The method of internal standards was used to quantify the amount of quartz present in Glaze B by XRD.⁴⁰ Fluorite (CaF_2) was used as the internal standard due to the fact that its characteristic X-ray peaks do not obstruct or confound the quartz peak information.⁴¹

2.7.2.1 Sample Preparation

Quantitative XRD samples were prepared by grinding the glass with a mechanical mortar and pestle. The powder was then mixed with 10wt% fluorite in an alumina mortar and pestle by hand. To ensure complete homogeneity, the powder was then wet mixed by hand using acetone and a Teflon spatula, and once dry, was then ground again. The powder mixture was then analyzed using XRD (Siemens D500 Goniometer, CuK α radiation, Alfred University, Alfred, NY). The parameters used were: 2 θ range: 19-57°, step size: 0.04°, and dwell time: 4 seconds.

2.7.2.2 Profile Fitting

Three quartz and fluorite peaks were chosen for use in the quantitative analysis. Table 2-VIII lists the peaks and their corresponding 2 θ ranges that were used.⁴¹

Table 2-VIII. 2 θ Ranges for Quantitative XRD Analysis

Phase	2 θ Range	2 θ Peak
Quartz	19-22	20.84
	38.2-41.5	38.38
	49-51	49.80
Fluorite	27-29.5	28.24
	46-48	46.97
	54.5-57	55.74

The following parameters were used in the Jade (Version 6.0, Materials Data, Inc.) profile-fitting function. The Background Fitting Dialog Window was set up for a medium background with medium sampling and automatic noise determination. The vertical background was set to 0%, the background fit was linear, K α_2 peaks were included, and individual profile peaks were used. The Peak Search and Labeling Dialog boxes were selected to ensure that the filter length was set at eleven points with a three-sigma threshold and an intensity

cutoff of 1%. One of the characteristic peaks was then chosen using the Zoom Window. The Profile Fitting Dialog starting-shape-factor settings were adjusted to 1.5 for the Pearson-VII, and 0.5 for the Pseudo-Voigt function. The skew was set at zero. In the profile window, position, height, FWHM, skew, and shape were all refined. This was done by altering between the Pearson-VII function and the Pseudo-Voigt function until a minimal residual (R%) was achieved. The 2θ peak position, height intensity, and area intensity were recorded. Area intensity was the only measurement used in the calculations.

2.7.2.3 Percent Quartz Calculation

The area intensities from the characteristic quartz peaks were added together and then divided by the combined area intensity of the fluorite peaks. The result is then multiplied by the wt% of the internal standard in that sample, 10 in this case, since 10 wt% internal standard was added. Figure 2.7 is the calibration curve for quartz. The addition of the internal standard “dilutes” the sample, and therefore, the result given by the calibration curves. To correct this, the resulting wt% crystalline phase was divided by 0.9. This correction will then yield the accurate amount of quartz present in the sample.

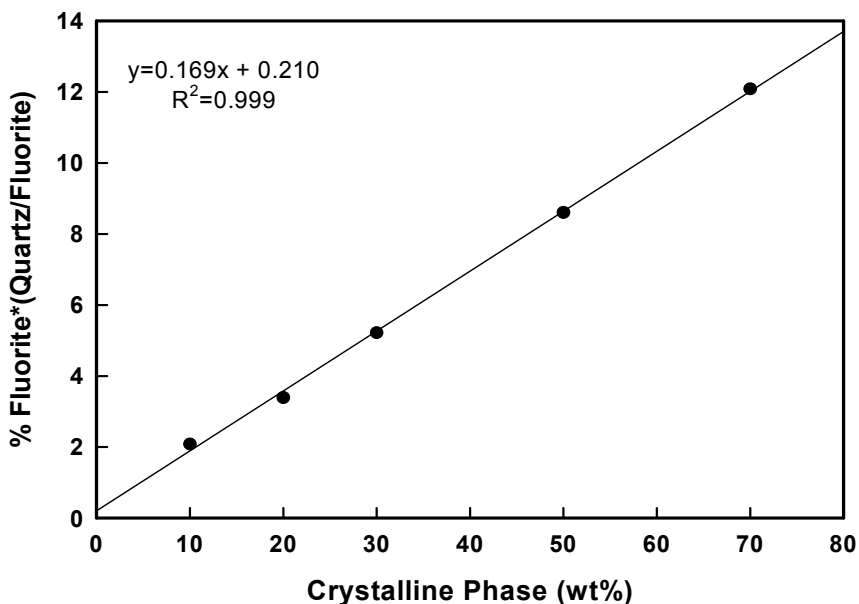


Figure 2.7. Quantitative XRD internal standard calibration curve for quartz.⁴¹

3 RESULTS AND DISCUSSION

3.1 Determination of Coefficient of Thermal Expansion Values

Coefficient of thermal expansion (CTE) values published in literature can be misleading if the temperature range over which it was calculated is not also listed. Several temperature ranges are used by various people. The average volumetric CTE over a temperature range T_1 to T_2 is given by the equation:⁴²

$$\text{CTE} = \frac{V_2 - V_1}{V_1(T_2 - T_1)} \quad (6)$$

where V_2 and V_1 are the volumes of the material at temperatures T_2 and T_1 , respectively. If the CTE curve is linear below T_g , the average CTE is a constant value and is referred to as the linear CTE of the specimen. Industrially, CTE values are often calculated over a temperature range of 200-500°C, due to the fact that this range is normally linear.⁴³ Using a temperature range only up to 500°C can potentially be dangerous. If the glaze has a $T_g > 500^\circ\text{C}$, erroneous results can occur; i.e., a glaze that should be placed in compression at 500°C but has a T_g that is much higher and a larger CTE value than the body at T_g may actually be placed in tension.¹¹

Another typical temperature range that is stated is from $\sim 25^\circ\text{C} - T_g$. There is a temperature range over which a glass gradually transforms upon cooling from a supercooled liquid to a glassy state. The glass formation temperature (T_g) is usually described as the intersection of the glassy state line with the tangent to the steep portion of the state curve in the transition range in the volume-temperature curve. The T_g is also sometimes stated as the temperature at which the viscosity of the glass is $10^{12} \text{ Pa}\cdot\text{s}$.^{42,44}

The importance of stating the exact temperature range over which the CTE has been calculated is evident. Significant differences in CTE values can be obtained when different temperature ranges are used. Each of these values are dependent on the composition of the glaze.

3.2 CTE as a Function of Composition

Initial thermal expansion values were disregarded, and dilatometer experiments were performed again on all glazes, due to the fact that the results were not reliable. The initial values were considered unreliable since they did not correspond with results that had previously been deemed correct. Significantly different values were obtained in the second trials. These are the values listed in Table 3-I. Figure 3.1 shows how CTE is affected by the $\text{SiO}_2:\text{Al}_2\text{O}_3$ ratio and the amount of SiO_2 . The CTE value for Glaze B does not correlate with the amount of silica present in the glaze. Glaze B has the highest silica level, verified by chemical analysis (Appendix A), and, therefore, should have the lowest CTE. The increase in thermal expansion seen in Glaze B can be attributed to the fact that there are undissolved quartz particles present in the glaze, as verified by XRD. The presence of undissolved quartz particles causes the thermal expansion of a glaze to increase significantly due to the fact that quartz particles have a higher thermal expansion than the glass phase. Glaze B was then fired to a temperature of 1350°C , with a dwell time of 1 hour, to dissolve all of the quartz particles. Thermal expansion measurements were then performed on this sample. As predicted, the thermal expansion of the glass significantly decreased when the quartz particles were dissolved.¹⁰ The same case can be made for Glaze F having a higher thermal expansion than the base glaze even though it has a greater amount of SiO_2 .

The glass transition temperature (T_g) and the softening point (T_s) of the glazes are also listed in Table 3-I.

Table 3-I. CTE, T_g , and T_s Values of Glazes and Bodies

Sample	CTE ₂₀₀₋₅₀₀ ($\times 10^{-6}/K$)	SD ₂₀₀₋₅₀₀ ($\times 10^{-6}/K$)	CTE _{50-Tg} ($\times 10^{-6}/K$)	T_g ($^{\circ}C$)	T_s ($^{\circ}C$)
Glaze A	7.26	0.31	7.45	744	794
Glaze B	6.96	0.53	6.85	743	825
Glaze B(1350)	5.38	0.11	5.53	747	838
Glaze C	6.19	0.29	6.17	758	798
Glaze D	6.72	0.14	6.80	748	799
Glaze E	6.03	0.27	5.90	753	811
Glaze F	5.97	0.06	6.16	766	825
Base Glaze	5.53	0.08	5.34	756	810
Alumina Body	6.87	0.13	-	-	-
Silica Body	6.48	0.08	-	-	-

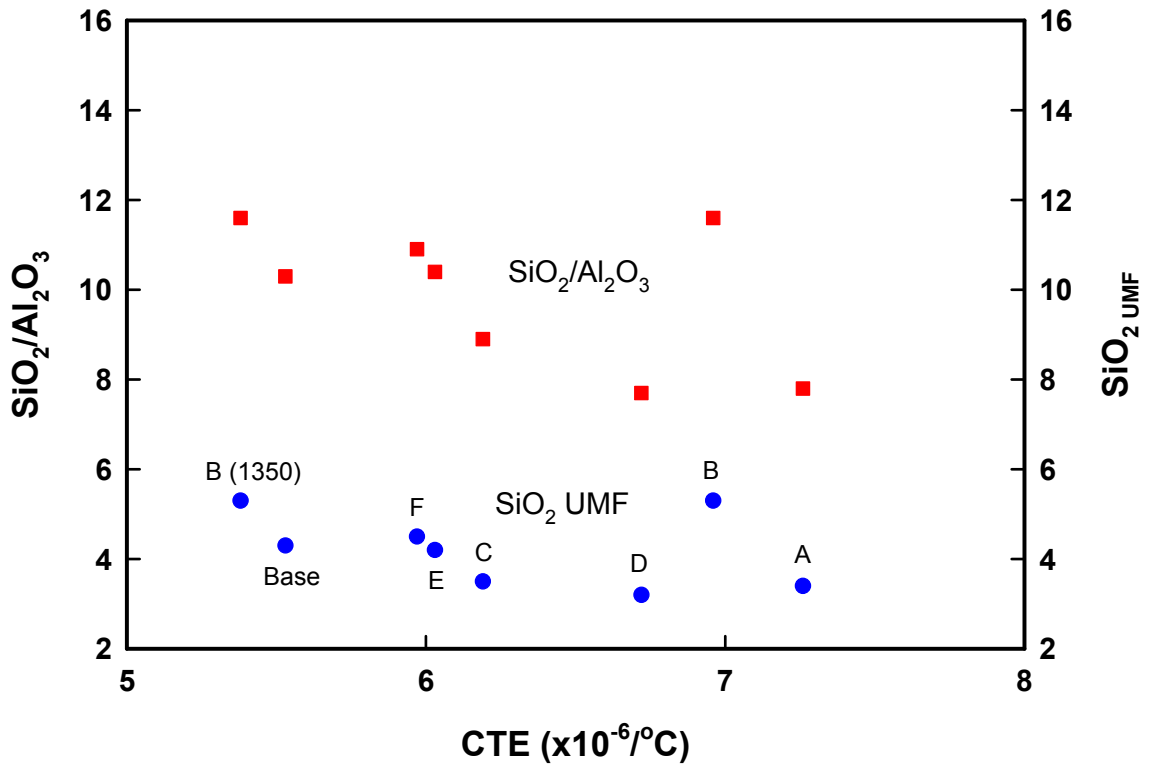


Figure 3.1. Effect of SiO_2/Al_2O_3 ratio and the amount of SiO_2 on the CTE of the glaze.

CTE values were calculated over various temperature ranges to show that there was little change over the various ranges. CTE curves of the Glasses A, B, C, and D are shown in Figure 3.2, while Glasses E, F, Base and B(1350) are shown in Figure 3.3. CTE curves for the bodies can be found in Figures 3.2 and 3.3. Only half of the glasses are shown in each plot for clarity reasons.

The silica body shows three regions of varying slopes. This is due to the quartz transformation. These three regions include (1) practically constant slope until approximately 560°C, (2) an increase in slope above 560°C due to the transformation of α -quartz to β -quartz, and (3) a decrease in slope at approximately 610°C back to roughly the original value. The amount of silica in the body and the maturing temperature of the body dictate the amount of transformation effect.⁴⁴

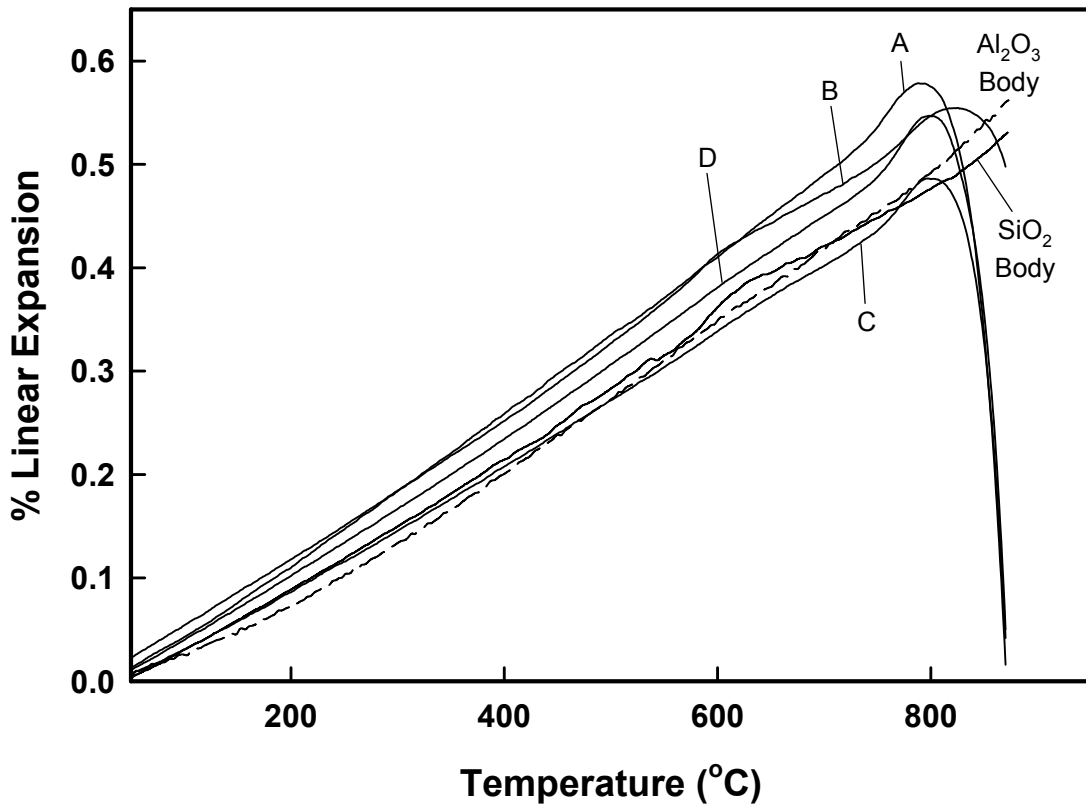


Figure 3.2. CTE curves for Glasses A, B, C, D and the bodies.

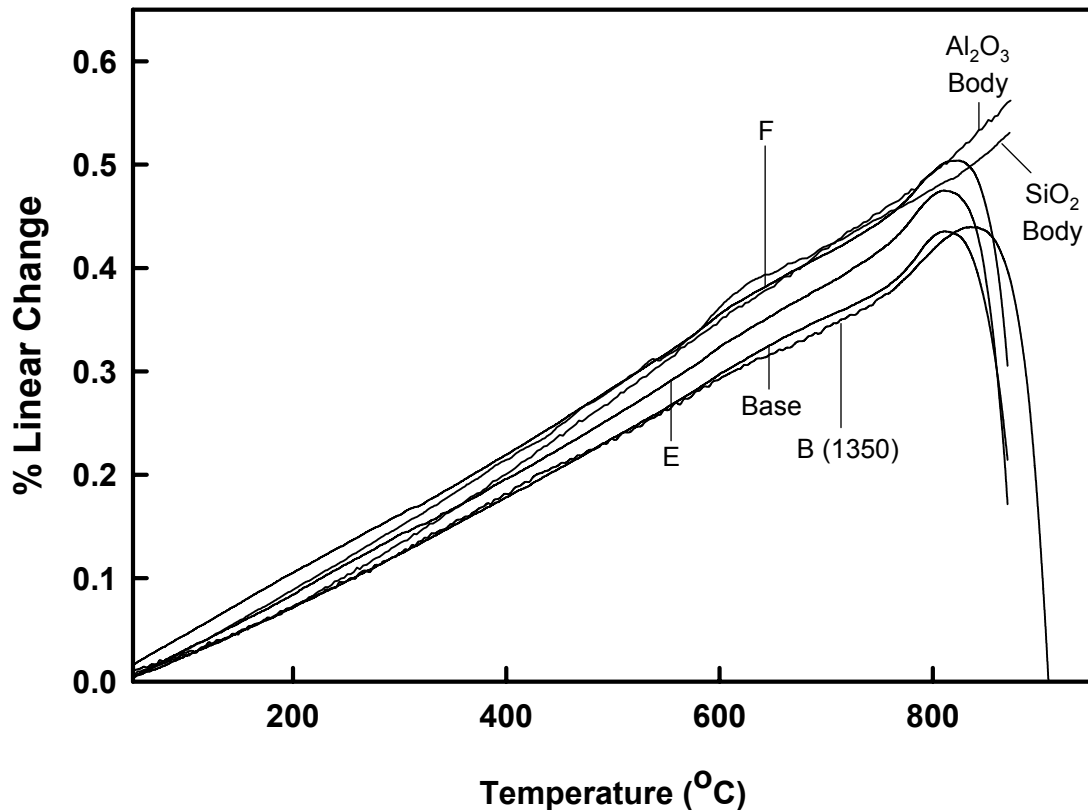


Figure 3.3. CTE curves for Glasses E, F, Base, and B(1350) and the bodies.

3.2.1 Qualitative XRD Analysis

XRD was used to determine if there was any undissolved quartz present in the glaze. Glazes B and F contained undissolved quartz. XRD patterns for these glazes are shown in Figures 3.4 and 3.5, respectively. The XRD pattern of Glaze B fired to 1350°C showed the presence of just a small amount of undissolved quartz. This pattern is located in Figure 3.4. Glazes C, D, E, F, and the base glaze all showed the presence of zircon as the crystalline species. This was expected, since zircon was added as a raw material to the glaze. Glaze A had no crystalline species present, as shown by the large amorphous hump found for the XRD pattern. XRD patterns for Glazes A, C, D, E, and the Base glaze are located in Appendix D.

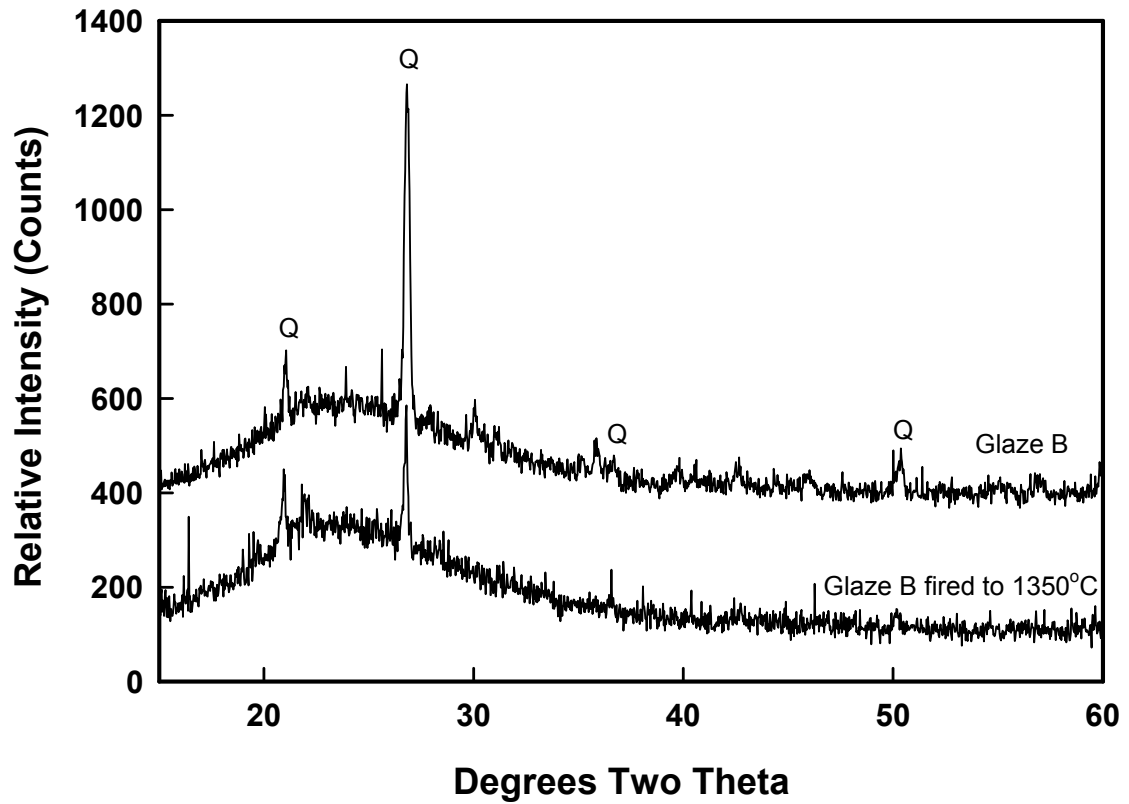


Figure 3.4. XRD pattern of Glaze B showing the presence of undissolved quartz, and XRD pattern of Glaze B fired to 1350°C with an insignificant amount of undissolved quartz present. The quartz peaks have been labeled (Q).

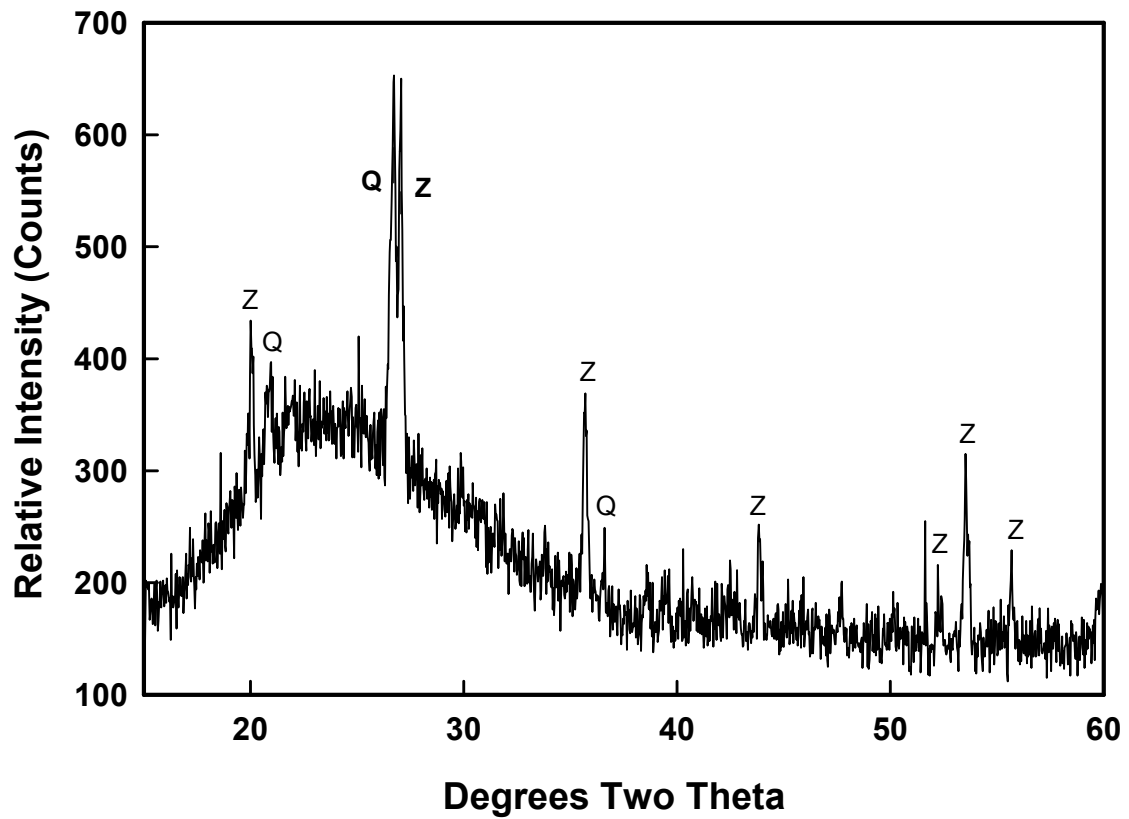


Figure 3.5. XRD pattern of Glaze F showing the presence of undissolved quartz particles. Quartz (Q) and zircon (Z) peaks are labeled.

XRD was performed on Glaze B after application on both bodies. XRD patterns for both bodies can be found in Figure 3.6. In both cases a significant amount of quartz is present, indicating that not all of the quartz particles were dissolved during firing.

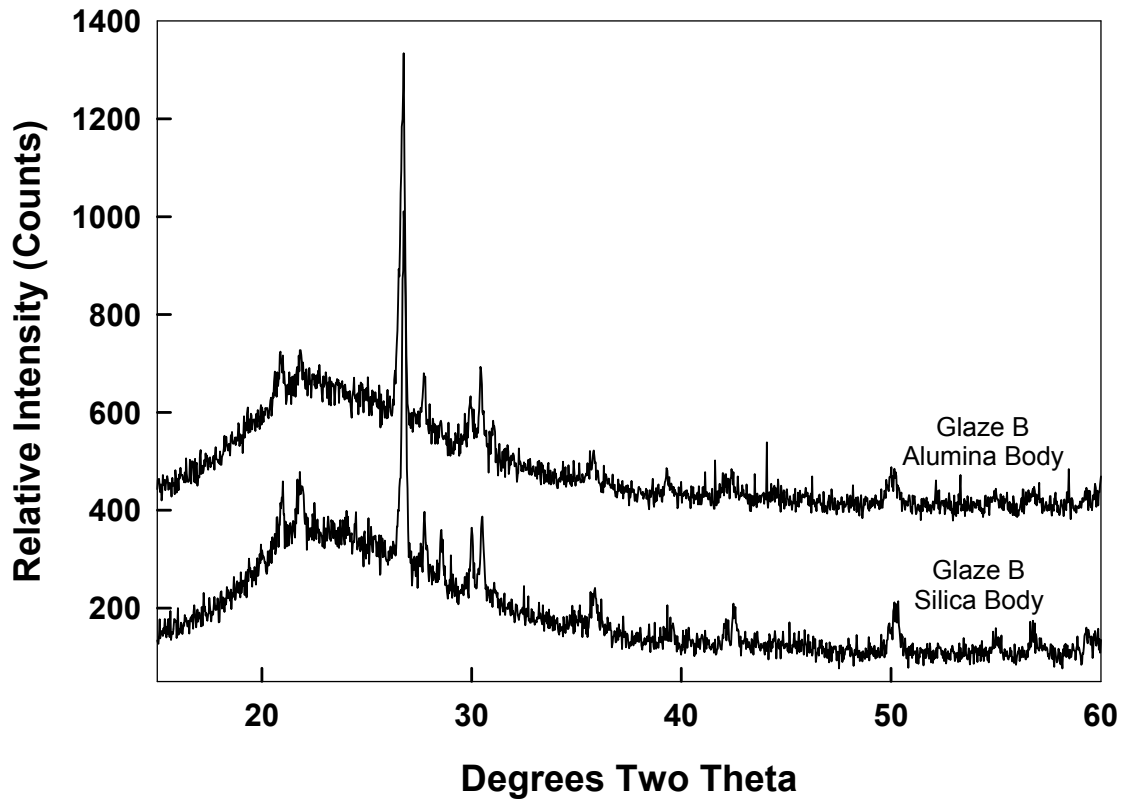


Figure 3.6. XRD pattern of Glaze B applied to the alumina and silica bodies showing the presence of undissolved quartz particles.

3.2.2 Quantitative XRD Analysis

The diffraction patterns of the initial Glaze B and the one fired to 1350°C, mixed with 10wt% CaF₂, can be found in Figure 3.7. The initial Glaze B shows a significant amount of undissolved quartz present. Based on quantitative analysis, it was determined that ~4 % quartz was present after firing. Once Glaze B was fired to 1350°C, no significant amount of quartz was present in the glaze; therefore, no apparent quartz peaks were present in the diffraction pattern. This supports the theory that undissolved quartz increases the glaze CTE.

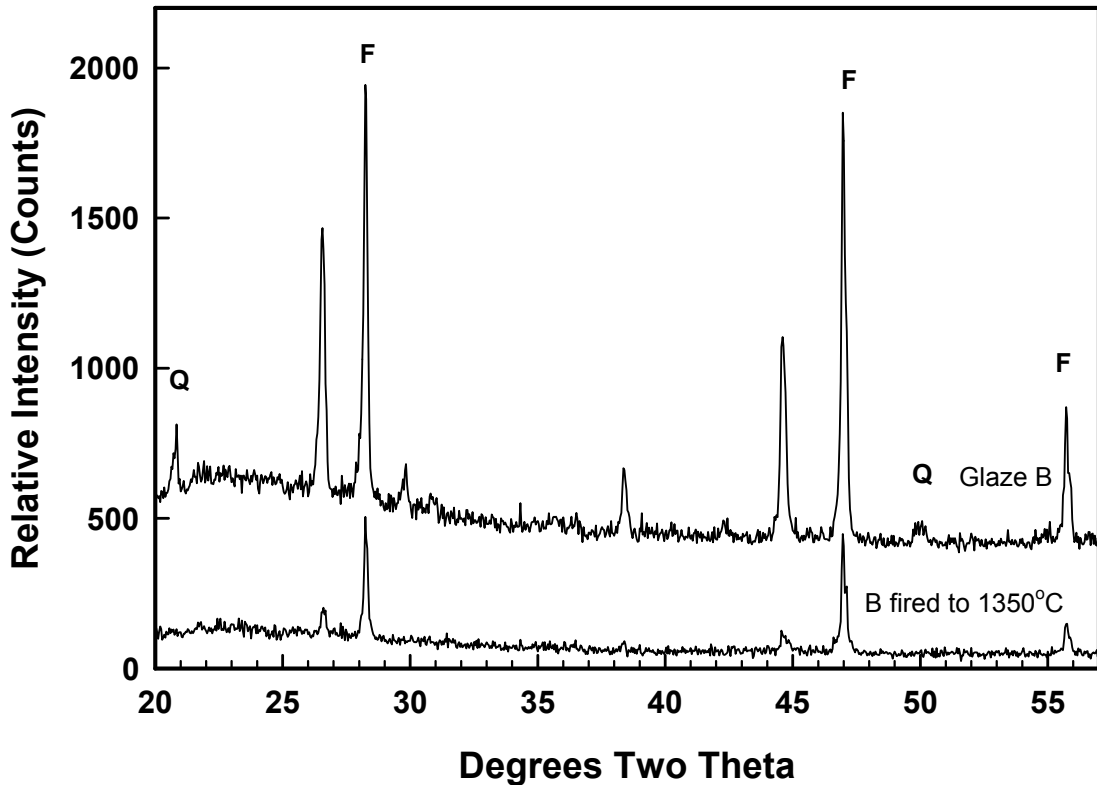


Figure 3.7. XRD pattern of Glaze B and Glaze B fired to 1350°C with fluorite added. Quartz (Q) and CaF₂ (F) peaks used in analysis are labeled.

3.3 Strength Testing

3.3.1 Effect of Glaze Composition

3.3.1.1 Silica Body

The samples glazed with the base glaze resulted in the highest strength values. Samples glazed with Glaze B(1350) had a glaze with more compression present than those samples glazed with the Base glaze, but there was not a statistical increase in strength in those samples. It is believed that an apparent maximum in strength, of 97 MPa, has been reached, and increasing the CTE mismatch between the body and glaze will not lead to an increase in strength, but may eventually lead to a decrease in strength due to shivering. The strength of the samples was maximized at a thermal expansion mismatch level of $0.93 \times 10^{-6}/K$.

Samples glazed with Glaze A, which had the least amount of compression present in the glaze, resulted in the lowest strength values. The amount of compression present in the glaze correlated with the strength of the sample for the once-dipped samples, except for one glaze. Rods glazed with Glaze F, which should have provided the second greatest strength values based on the amount of thermal expansion mismatch between the body and glaze, actually only gave average strength values. This was attributed to the large size of the fracture origins. Figure 3.8 shows how the amount of thermal expansion mismatch between the body and glaze affects strength. The twice-dipped Glaze A samples crazed, and were therefore excluded from the strength plot, and no samples twice-dipped with Glaze B(1350) were tested.

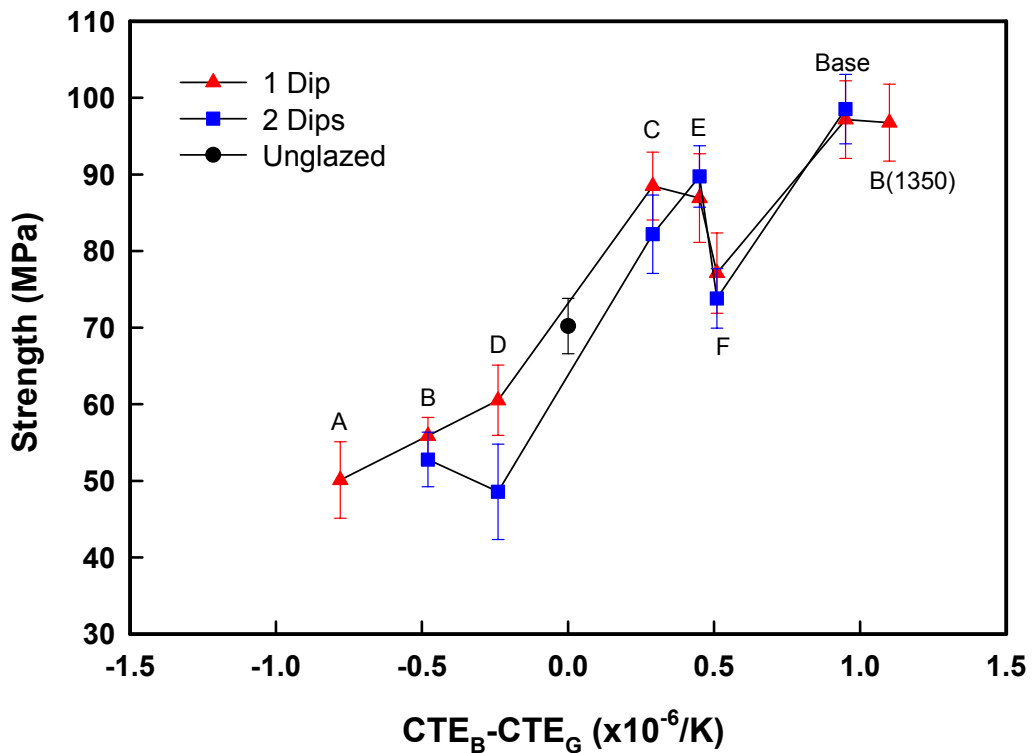


Figure 3.8. The effect of thermal expansion mismatch between the body and glaze on measured strength for the silica body.

Rods glazed with Glazes A, B and D gave strength values lower than that of the unglazed samples. Based solely on thermal expansion values, these glazes are in tension. This result would then be expected. All other glazes gave an increase in strength of ~9-28% over that of the unglazed samples.

3.3.1.2 Alumina Body

Initial results showed that the base glaze gave the highest strength values, and also had the greatest amount of theoretical glaze stress present. Glaze A again gave the lowest strength values. The twice-dipped Glaze A and D samples showed the existence of crystals in the glaze, and were therefore omitted from the strength plots. The samples glazed with Glaze B(1350) were also omitted from the strength plot because of excessive amounts of large pores at the glaze/body interface, which can be seen in Figure 3.9. This was attributed to a surface layer being present on the body and the glaze did not adhere well during application. Figure 3.10 shows how the amount of thermal expansion mismatch between the body and glaze affects the strength of the samples. Highest strengths were achieved when the mismatch between the body and glaze reached a level of $1.13 \times 10^{-6}/K$. This corresponded to a maximum strength value of 161 MPa. Rods dipped with Glazes A, B, and D all provided strength values lower than these of the unglazed samples. All other glazed rods resulted in an increase in strength of ~17-20% of that of the unglazed samples.

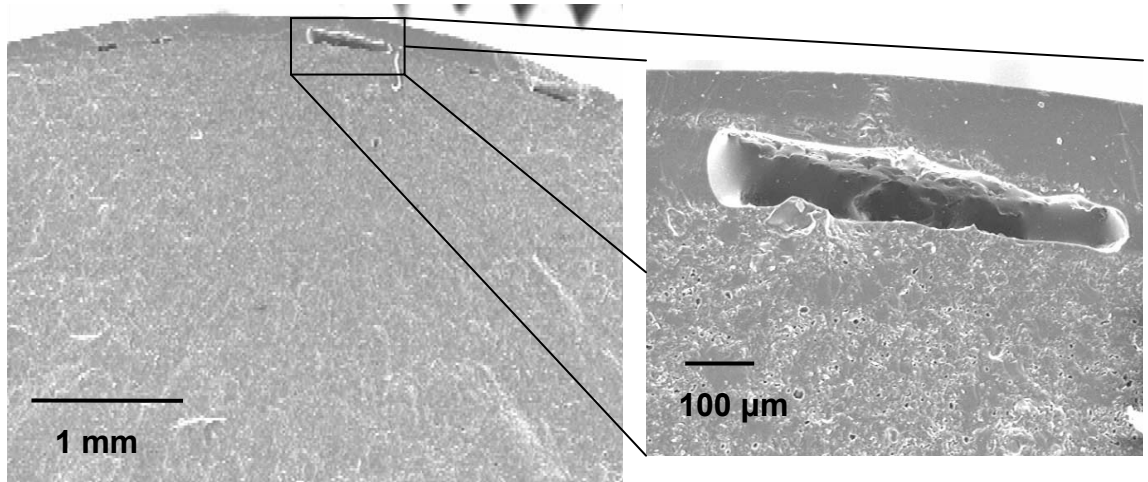


Figure 3.9. SEM micrograph of an alumina-body sample, glazed with Glaze B(1350), which shows large pores at the glaze/body interface caused by a reaction taking place due to the fact that a surface layer was present on the body.

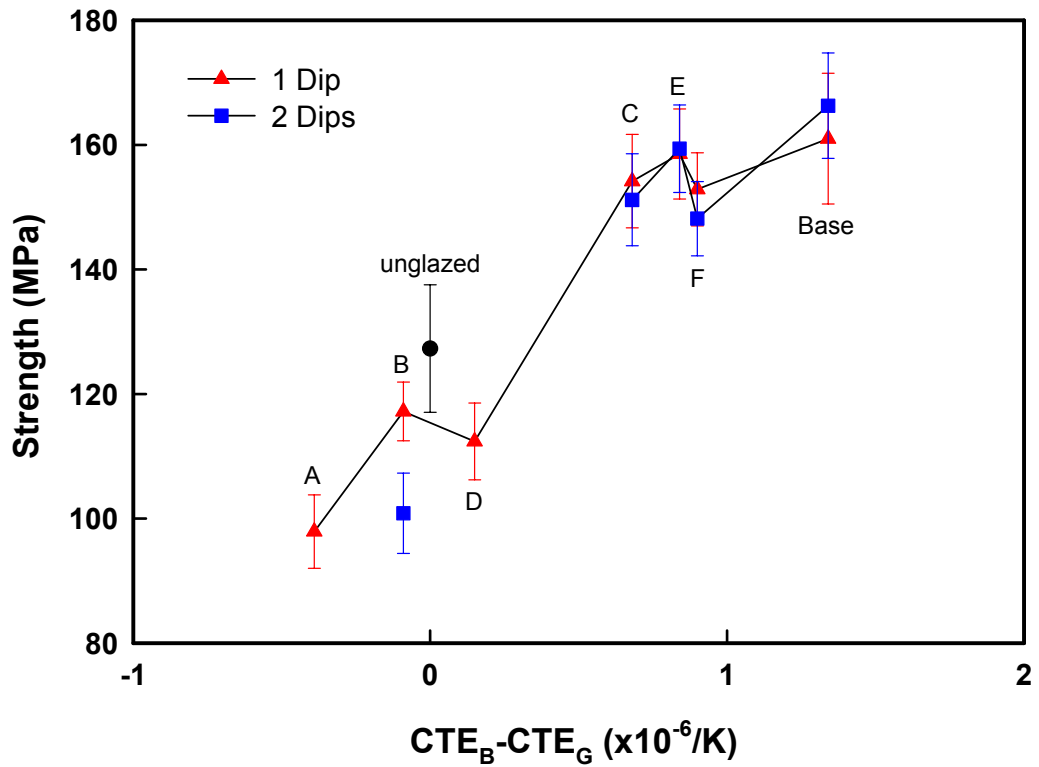


Figure 3.10. The effect of thermal expansion mismatch between the body and glaze on the measured strength of the alumina body.

3.3.1.3 Effect of CTE Mismatch on Normalized Strength

Figures 3.11 and 3.12 show how thermal expansion mismatch affects the measured strength when the strengths have been normalized to the Young's Modulus of the silica body and alumina body, respectively. The strength of the samples for each body has been normalized to the respective Young's Modulus of each body. This was done, because the Young's Modulus of the body contributes to the overall strength of the piece. Once the strengths have been normalized, it is possible to compare different bodies. A linear regression line was fit to the data, and it is shown that strength can be estimated if the amount of thermal expansion mismatch is known. The strength of the silica body samples can be estimated by the equation:

$$\frac{\sigma}{E} = 3.2 \times 10^{-4} (\Delta CTE) + 8.51 \times 10^{-4} \quad (6)$$

The strength of the alumina body samples can be estimated by the equation:

$$\frac{\sigma}{E} = 3.2 \times 10^{-4} (\Delta CTE) + 9.58 \times 10^{-4} \quad (7)$$

The unglazed alumina body sample is offset from the regression line. This was attributed to the surface layer that can be present on the body due to the alignment of clay particles during extrusion. It is shown that when the strength of the pieces has been normalized to the Young's Modulus of the respective body, both bodies behave similarly. This is proven by the fact that both regression lines have the same slope.

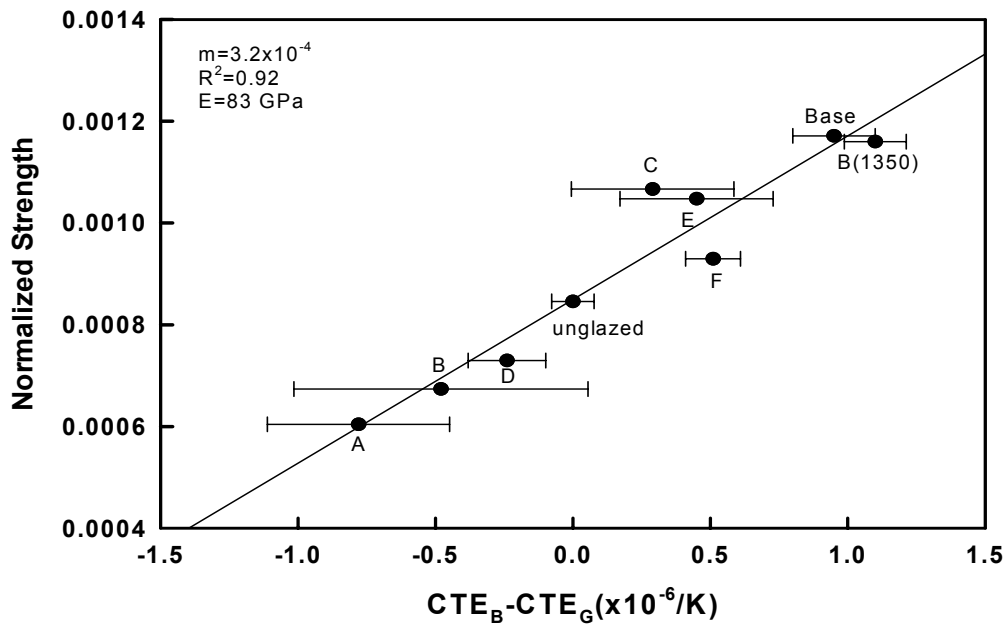


Figure 3.11. The effect of thermal expansion mismatch between the body and glaze when the measured strength has been normalized to the Young's Modulus of the silica body.

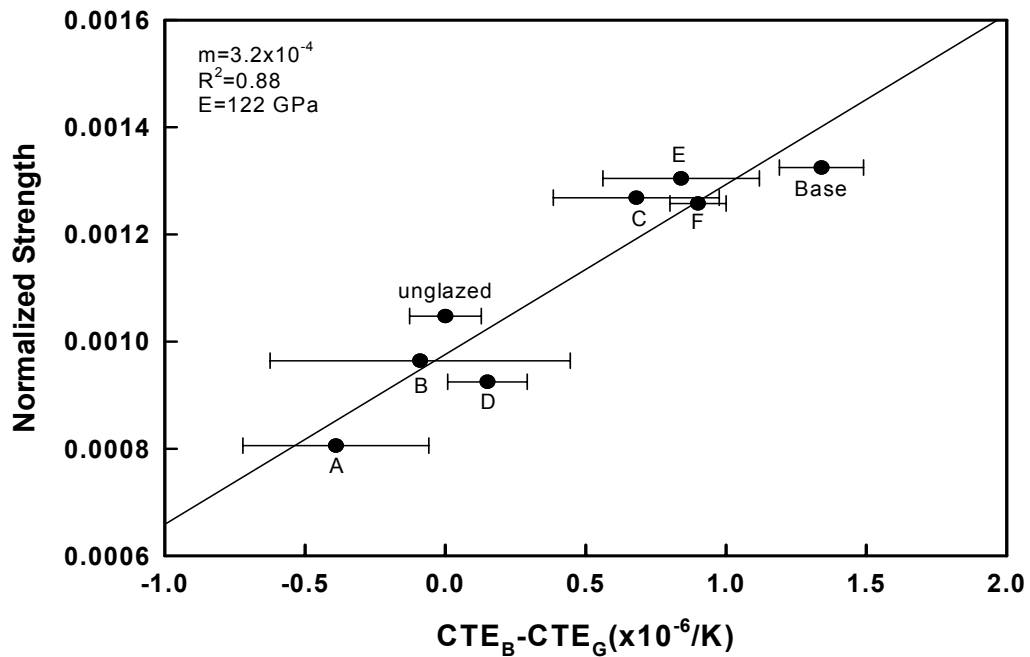


Figure 3.12. The effect of thermal expansion mismatch between the body and glaze when the measured strength has been normalized to the Young's Modulus of the alumina body.

3.4 Effect of Glaze Thickness

From the theoretical glaze calculations, the double-dipped samples for both bodies should have lower strengths. This was not always true. For the silica body, glaze thickness had no statistical effect on strength for the rods glazed with the Base glaze and Glaze E. For the alumina body, glaze thickness had no statistical effect on the rods glazed with the Base glaze and Glazes C and E. All statistical values were determined with 95% confidence, using the analysis of variance. Table 3-II lists which glazes had a statistical effect on strength.

Table 3-II. Strength Difference Caused by Glaze Thickness

Glaze	Statistical Difference in Strength Caused by Glaze Thickness	
	Silica Body	Alumina Body
A	Yes	Yes
B	Yes	Yes
C	Yes	No
D	Yes	Yes
E	No	No
F	Yes	Yes
Base	No	No

Rods glazed with Glaze A for both bodies provided a significant decrease in strength when the glaze thickness was increased. When a larger glaze thickness was applied to the silica body, all of the samples crazed. The thermal expansion mismatch between the body and the glaze was a negative number, i.e., ΔCTE was $-0.78 \times 10^{-6} \text{ K}^{-1}$. Consequently, the glaze was placed in tension. This would explain the drastic decrease in strength. These samples had fracture origins where the glaze crazed. The cracks became the critical flaw. When a larger glaze thickness was applied to the alumina body, the samples showed a significant amount of crystal growth in the glaze. Figure 3.13 shows these crystals, while the once-dipped samples showed apparent crystal growth as seen in Figure 3.14. Through the combinations of EDS and X-ray diffraction these

crystals were determined to be diopside ($\text{CaO}\cdot\text{MgO}\cdot 2\text{SiO}_2$). These graphs are located in Appendix E.

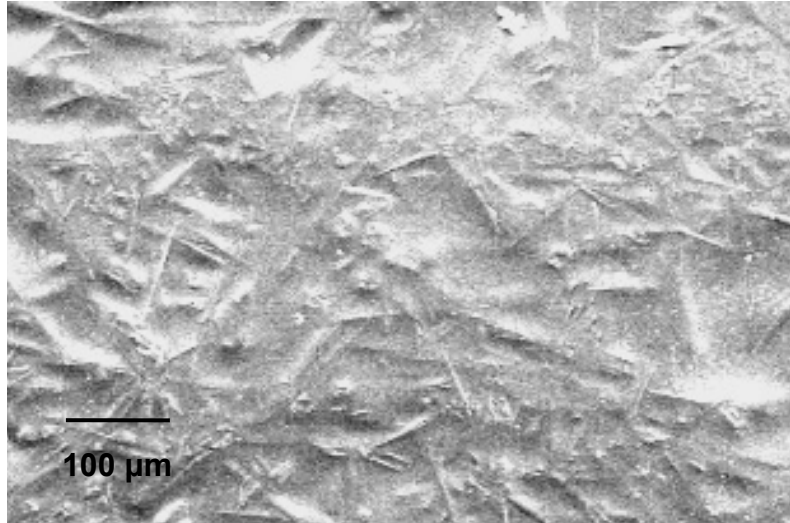


Figure 3.13. SEM photomicrograph of crystal growth seen on the glaze surface of Glaze A, twice-dipped on the alumina body. The crystals were determined to be diopside ($\text{CaO}\cdot\text{MgO}\cdot 2\text{SiO}_2$)

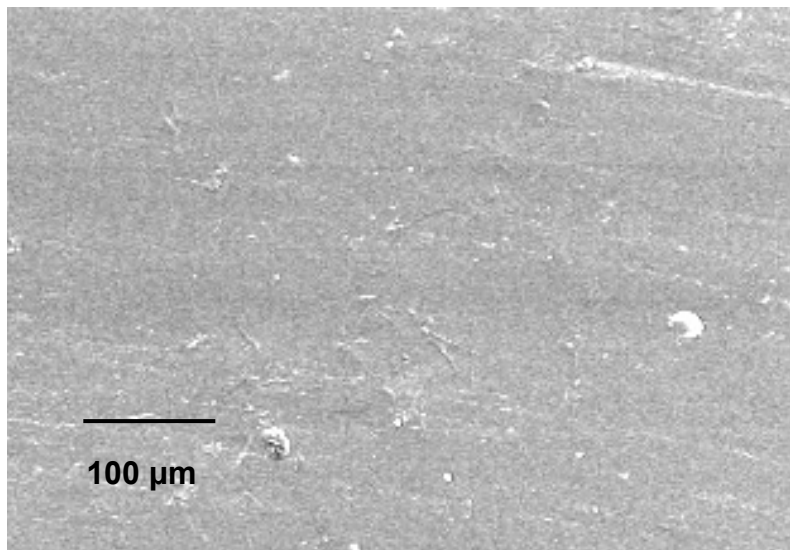


Figure 3.14. SEM micrograph of the glaze surface of Glaze A, once-dipped, on the alumina body. No crystal growth is apparent. The markings on the surface are scratches and dust from handling.

The rods twice-dipped with Glaze D on the alumina body showed the same type of crystal growth as the rods twice-dipped with Glaze A, but to a lesser degree. This again explains the drastic decrease in the strength of these samples. Again, the rods single-dipped with Glaze D on the alumina body did not show any crystal growth. Figures 3.15 and 3.16 show the glaze surfaces for both glaze thicknesses.

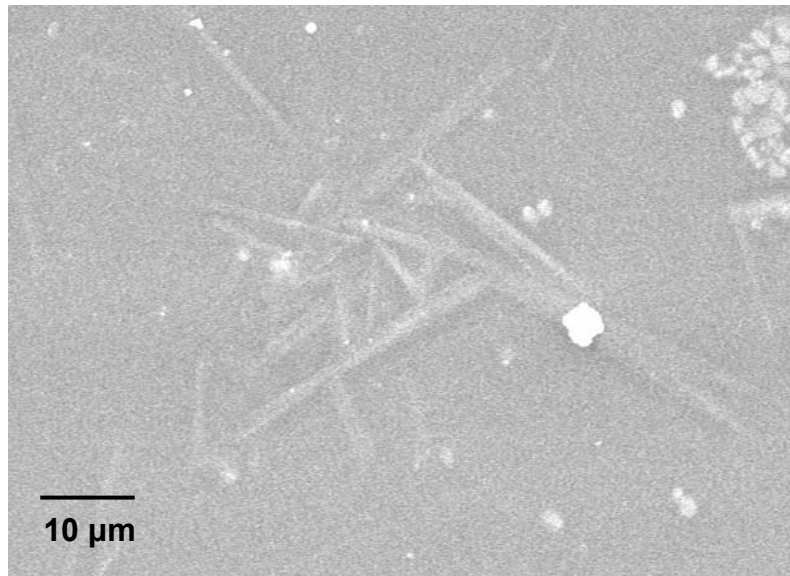


Figure 3.15. SEM photomicrograph of crystal growth found on the glaze surface of Glaze D, twice-dipped, on the alumina body. The elongated crystals were determined to be diopside. The cluster of crystals at the top right are zircon.

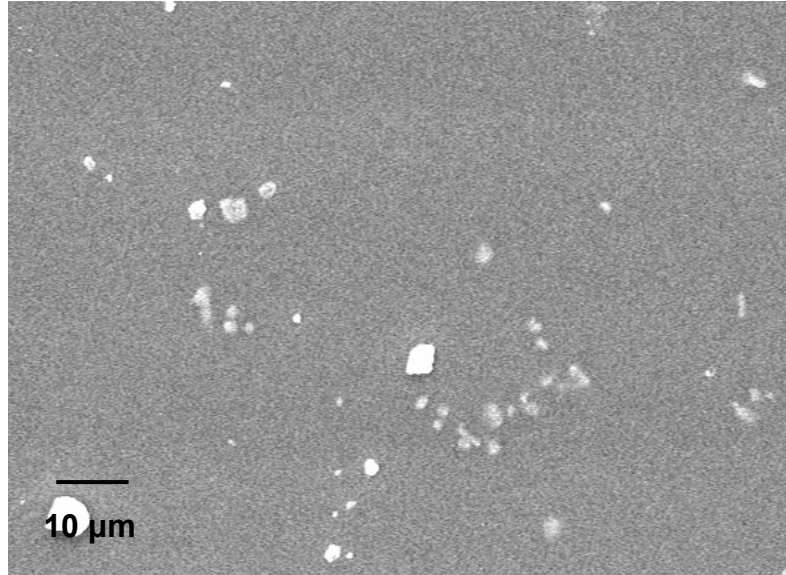


Figure 3.16. SEM photomicrograph of the glaze surface of Glaze D, once-dipped, on the alumina body. No significant amount of crystal growth is apparent, though a small amount of zircon is present.

3.5 Stress Calculations

3.5.1 Theoretical Stress Levels

A theoretical approach to estimate the amount of stress present in a glaze and body is to assume that the glaze stress is solely dependent on the restriction imposed on its expansion by its bond with the body.¹⁶ The amount of stress, in a cylinder, can be determined if it is assumed (1) that the elastic moduli and Poisson's ratios of the glaze and the body are the same, (2) that both the body and glaze are elastic and isotropic, and (3) that the temperature distribution is uniform. If any of these assumptions are invalid this method for determining the amount of stress present could provide incorrect or unreliable results. The amount of stress present in the glaze and body can then be determined by the equations:^{4,13}

$$\sigma_G = -(\alpha_B - \alpha_G)\Delta T \left(\frac{E}{1-\mu} \right) \left(\frac{A_B}{A} \right) \quad (8)$$

and

$$\sigma_B = (\alpha_B - \alpha_G)\Delta T \left(\frac{E}{1-\mu} \right) \left(\frac{A_G}{A} \right) \quad (9)$$

where:

α_B =coefficient of thermal expansion of the body

α_G =coefficient of thermal expansion of the glaze

ΔT =temperature difference between T_g of the glaze and the temperature where the stress is measured

E =Young's modulus

μ =Poisson's ratio

A =total cross-sectional area of the cylinder

A_B =cross-sectional area of the body

A_G =cross-sectional area of the glaze

Based on these theoretical calculations, the specimens with Glaze B(1350) have the largest amount of stress and those with Glaze A have the lowest for the silica body. The specimens with the Base glaze have the largest amount of stress present in the glaze, and those with Glaze A have the lowest for the alumina body. These values correlate with the strength values obtained from flexure testing. The samples that were dipped twice, which thus have a larger glaze thickness, have less stress in the glaze simply because the amount of stress distributed over a larger volume. Table 3-III is a list of the stress values present in the glaze and the body, where a negative sign indicates a state of compression.

Table 3-III. Theoretical Stress Values of the Specimens

Glaze	Silica Body		Alumina Body	
	σ_{Glaze} (MPa)	σ_{Body} (MPa)	σ_{Glaze} (MPa)	σ_{Body} (MPa)
A	55	-2	65	-2
A2	52	-5	61	-6
B	34	-1	30	-1
B2	32	-3	29	-3
D	17	-0.8	3	-0.1
D2	17	-1	3	-0.2
C	-21	0.4	-59	0.4
C2	-21	0.8	-58	2
E	-33	0.8	-77	0.5
E2	-32	1.6	-75	3
F	-38	0.9	-85	1
F2	-37	2	-82	4
Base	-70	1	-137	1
Base2	-68	4	-132	6

*2 after the glaze denotes the twice-dipped samples.

Figures 3.17 and 3.18 show how the amount of stress present in a glaze is dependent on the thermal expansion mismatch between the glaze and the body, for the silica body and alumina body, respectively. The greater the amount of mismatch, the greater the amount of stress present in the glaze. Table 3-IV shows that the body has much less stress present in it than the glaze. This is because the stress in the body is distributed over a larger volume than in the glaze. Based solely on the amount of stress present in the glaze, the silica samples glazed with Glazes A and B should have higher strength values than the alumina samples with the same glazes, but this is not the case, since alumina bodies have greater strengths than silica bodies.

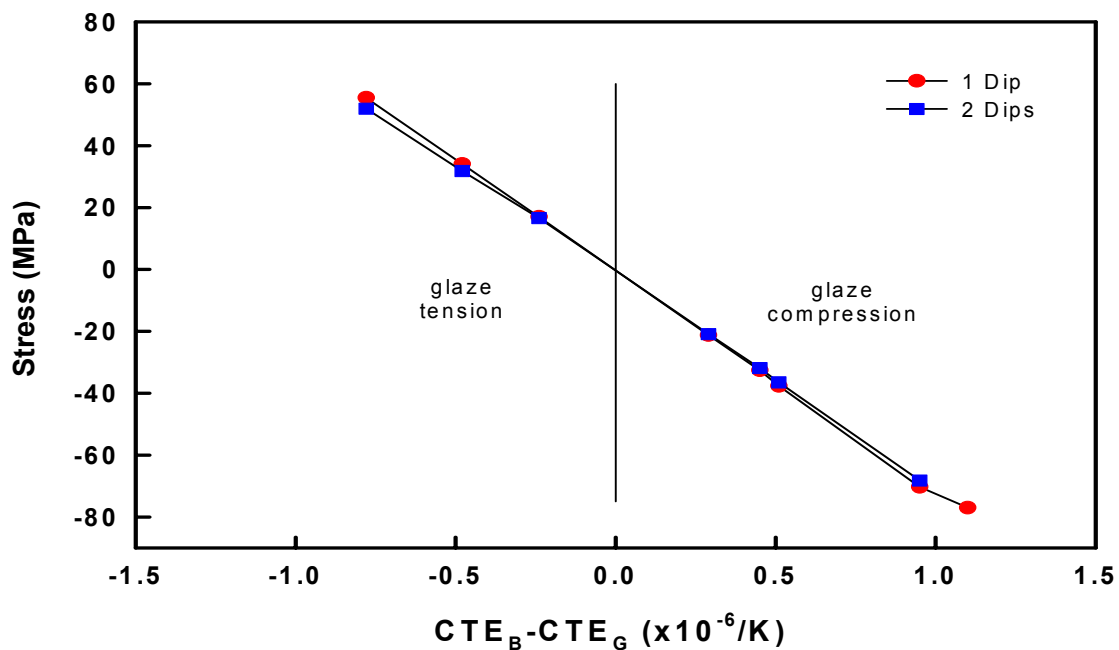


Figure 3.17. Theoretical stress levels present in the glaze based on the thermal expansion mismatch between the glaze and the silica body.

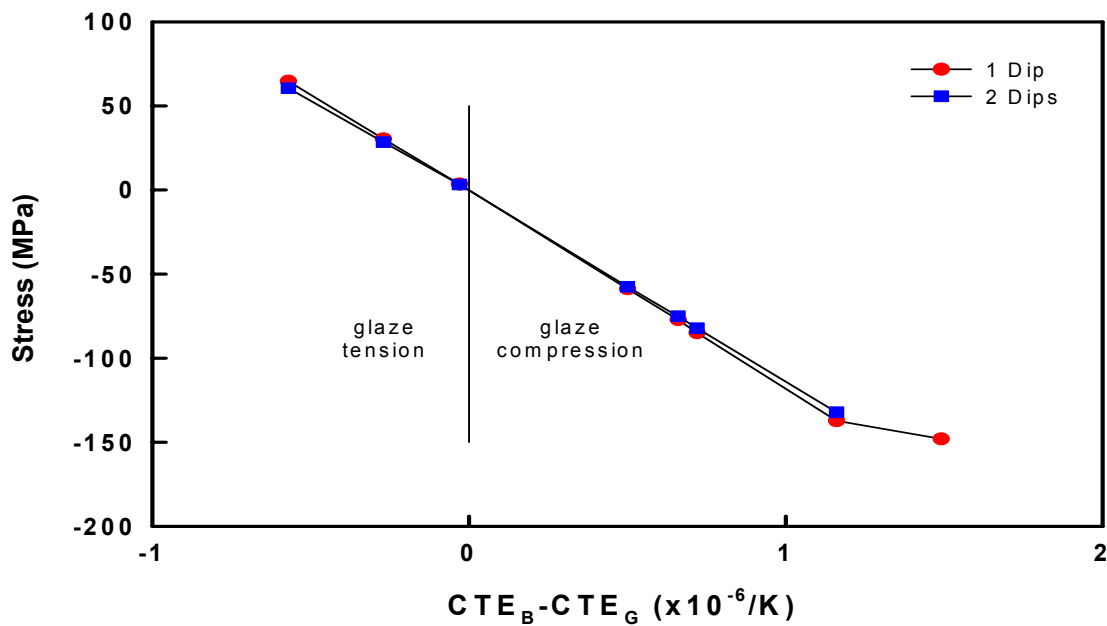


Figure 3.18. Theoretical stress levels present in the glaze based on the thermal expansion mismatch between the glaze and the alumina body.

3.5.2 Measured Glaze Stress Levels

The results of the measured glaze stress experiments were inconclusive. No correlation could be made between the strengths of the sample, calculated stress values, and the measured stress values, which can be seen in Figures 3.19 and 3.20. No values for Glaze B applied to either body are presented, because these samples broke during firing. A similar situation occurred on the alumina-body sample glazed with Glaze D. It is suggested that since a very thin cross-section of substrate was glazed, the bulk properties of the substrate are no longer observed; there are changes in the interaction between the glaze and substrate. The amount of residual stress is calculated by the formula:¹⁶

$$\sigma_{\text{sat}} = \frac{[E_c E_s (t_c + t_s)^4 + (E_c - E_s)(E_c t_c^4 - E_s t_s^4)]}{[6R E_s t_c t_s (t_c + t_s)]} \quad (10)$$

where:

σ_{sat} =residual stress

E_c =glaze elastic modulus

E_s =substrate elastic modulus

t_c =glaze thickness

t_s =substrate thickness

R =curvature of specimen from the "warp test"

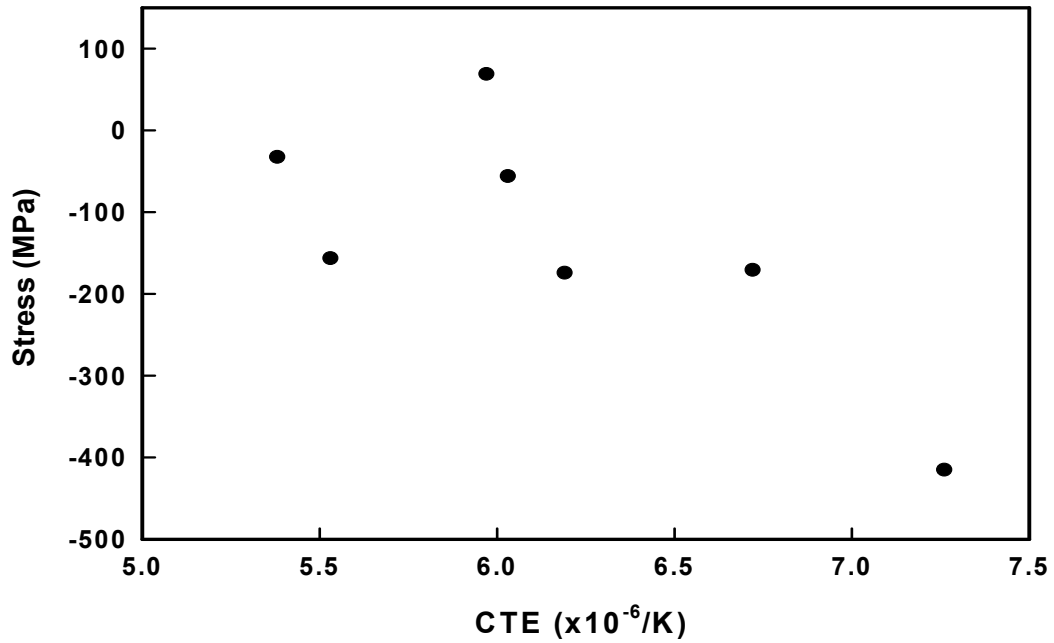


Figure 3.19. Calculated residual glaze stress levels, for the silica-body samples, determined using the "warp test" method.

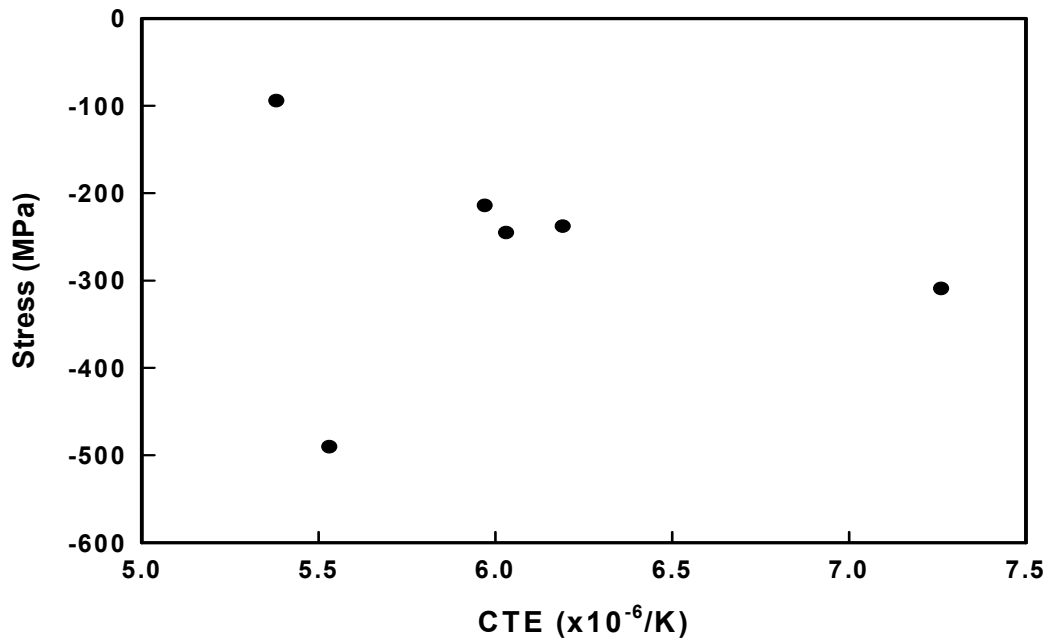


Figure 3.20. Calculated residual glaze stress levels, for the alumina-body samples, determined from the "warp test" method.

Figures 3.21 and 3.22 are images of the glazed substrates after firing. It can be seen in these figures that samples glazed with Glaze A warp the greatest amount, indicating the greatest amount of residual stress present in the glaze. This result contradicts all other results.

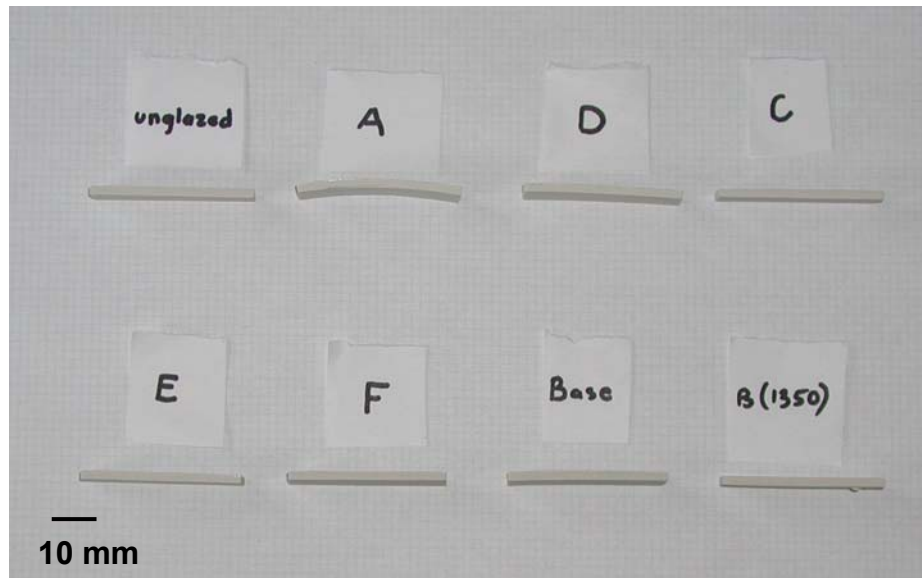


Figure 3.21. Image of "warp test" silica body samples.

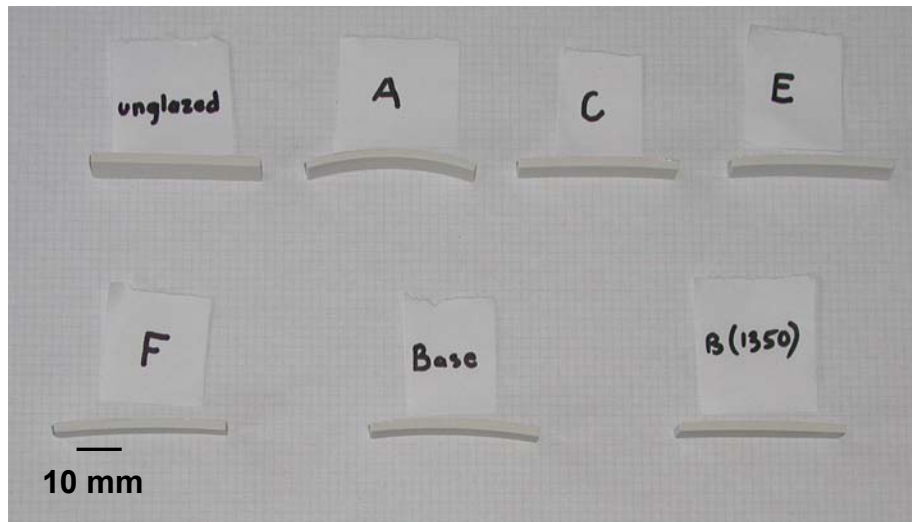


Figure 3.22. Image of "warp test" alumina body samples after firing.

3.6 Fracture Analysis

3.6.1 Comparison of Fracture Surfaces of the Bodies

Optical microscopes and SEM were used to locate and identify fracture origins of fractured samples. The silica-body samples produced mirrors that were larger than those of the alumina-body samples when comparing samples with the same glaze. This was expected, since the alumina-body samples had significantly larger strengths than the silica-body samples. The low-strength silica body samples had no mist hackle; i.e., the entire fracture surface was a mirror. This is caused by the fact that there was not enough stored elastic energy to create mist hackle. This can be seen in Figure 3.23.

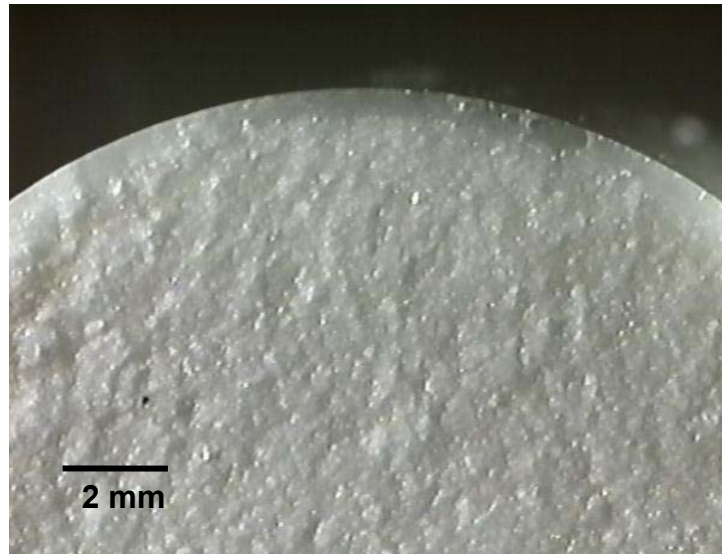


Figure 3.23. Low-magnification optical image of a typical low-strength silica sample, dipped with Glaze A, where the entire fracture surface was the mirror.

The high-strength silica-body samples had mirrors that were easily determinable with mist hackle surrounding them. Figure 3.24 is a representative sample of this situation.



Figure 3.24. A low-magnification optical image of a high-strength silica sample, dipped with the Base glaze, with a distinct mirror surrounded by mist hackle, with the fracture origin in the center of the mirror.

The low-strength alumina samples also did not exhibit any mist hackle. Once again the entire fracture surface was the mirror. This was caused for the same reasons as listed previously. The fracture surface was smooth and flat. Figure 3.25 shows an example of this situation.

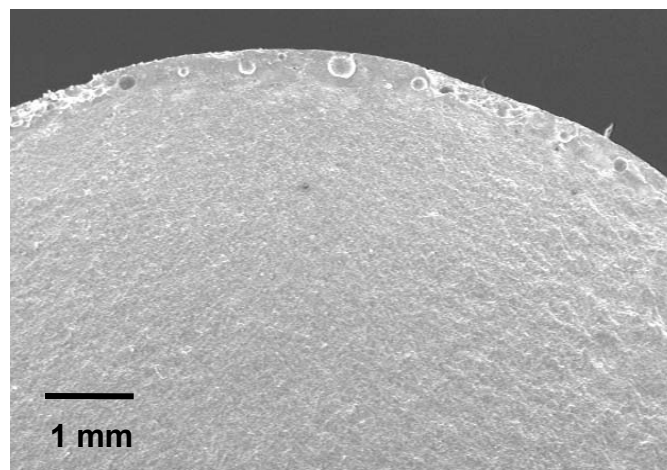


Figure 3.25. A low-magnification SEM image of a typical fracture surface of a low-strength alumina sample, dipped with Glaze B, where the entire fracture surface is the mirror.

The high-strength alumina-body samples had very distinct mirrors with surrounding hackle and fracture origins located near the middle of the mirror. The mirrors were generally small, since the samples had high strength, and strength is inversely related to the square root of the radius of the mirror, as shown is Equation 1. A representative sample of this case can be found in Figure 3.26.



Figure 3.26. A low-magnification optical image of a typical fracture surface of a high-strength alumina body sample, dipped with the Base glaze.

3.6.2 Comparison of Glaze Thickness for Each Body

The fact that there was no significant change in strength with the increase in glaze thickness for the base glaze can in part be explained by the strength-limiting flaws of the specimens. Both glaze thicknesses for the alumina body had similar fracture origins, and all of the fracture origins were found within the body. Examples of the fracture origins can be found in Figures 3.27 and 3.28.

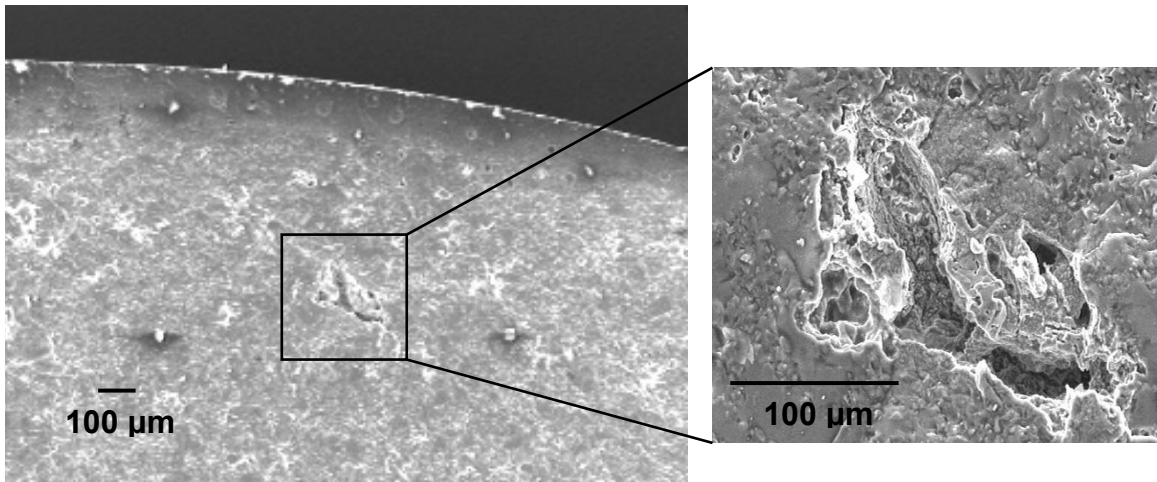


Figure 3.27. SEM photomicrograph of a typical fracture origin for alumina-body specimens with the Base glaze, once-dipped.

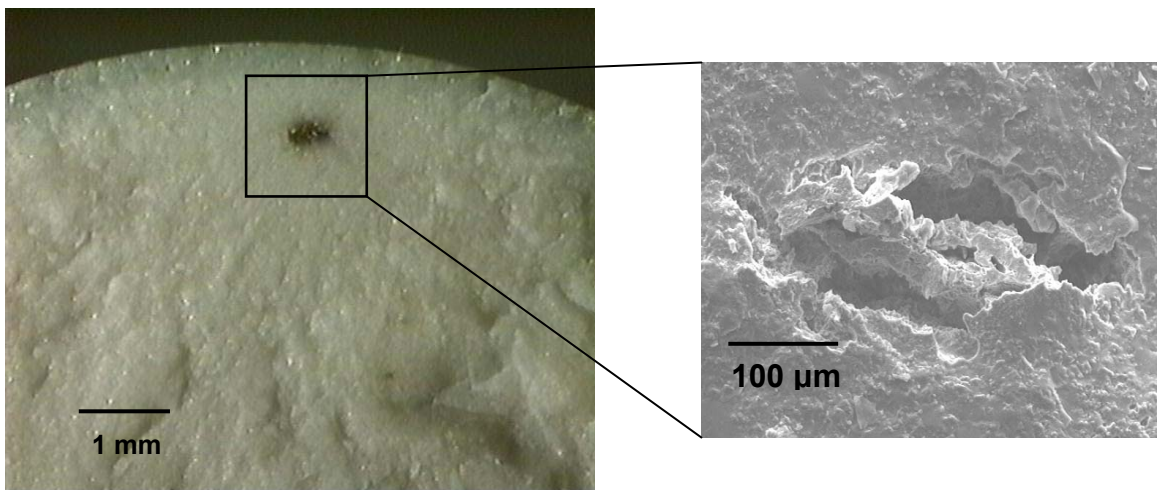


Figure 3.28. Low-magnification optical micrograph and a high-magnification SEM micrograph of a typical fracture origin for alumina-body specimens with the Base glaze, twice-dipped.

A similar situation occurred with both glaze thicknesses of Glaze E on the alumina body. Both cases had fracture origins just below the glaze/body interface. Typical fracture origins for both cases can be found in Figures 3.29 and 3.30.

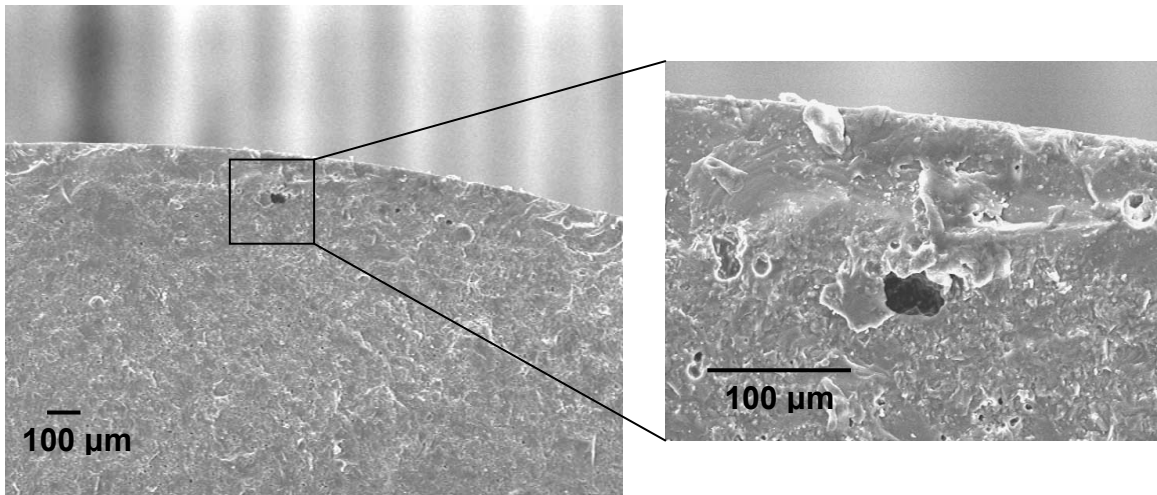


Figure 3.29. SEM micrograph of a typical fracture origin for alumina-body specimens with Glaze E, once-dipped.

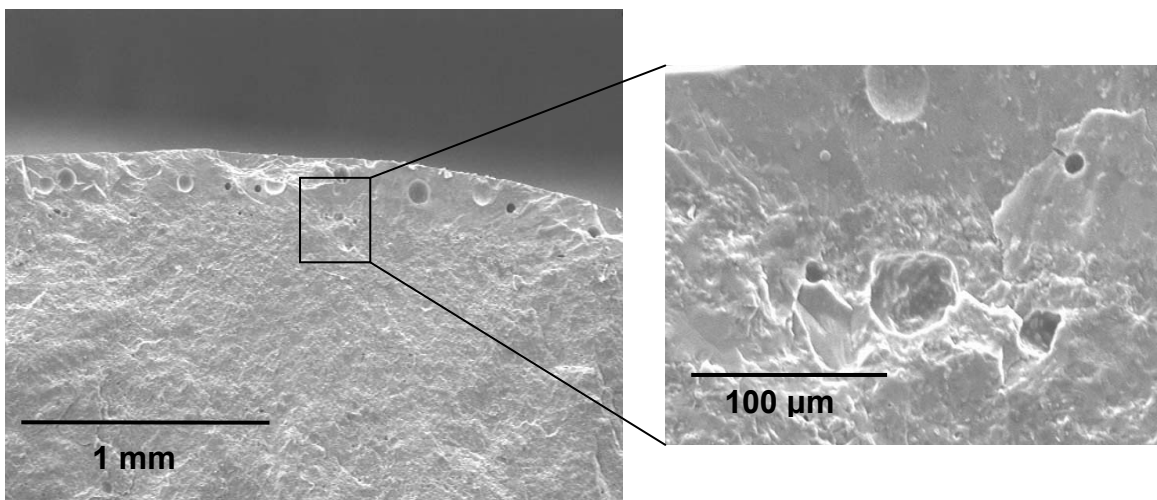


Figure 3.30. SEM micrograph of a typical fracture origin for alumina-body specimens with Glaze E, twice-dipped.

Glaze C had a statistically significant difference in strength when a thicker glaze was applied to the alumina body. The fracture origins shifted from the body, in the once-dipped samples, to the glazes, in the twice-dipped samples. The decrease in strength of the twice dipped samples is attributed to the fracture origins being larger than in the once-dipped samples. Figures 3.31 and 3.32 show typical fracture origins at the glaze/body interface for the once-dipped samples, and in the glaze for the twice-dipped samples.

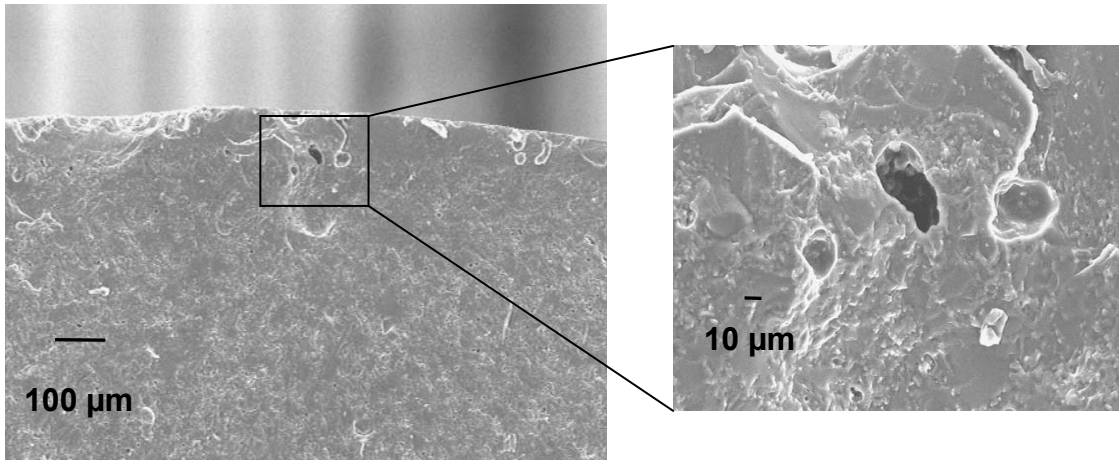


Figure 3.31. SEM micrograph of a pore at the glaze/body interface as the strength-limiting flaw for alumina-body specimens with Glaze C, once-dipped.

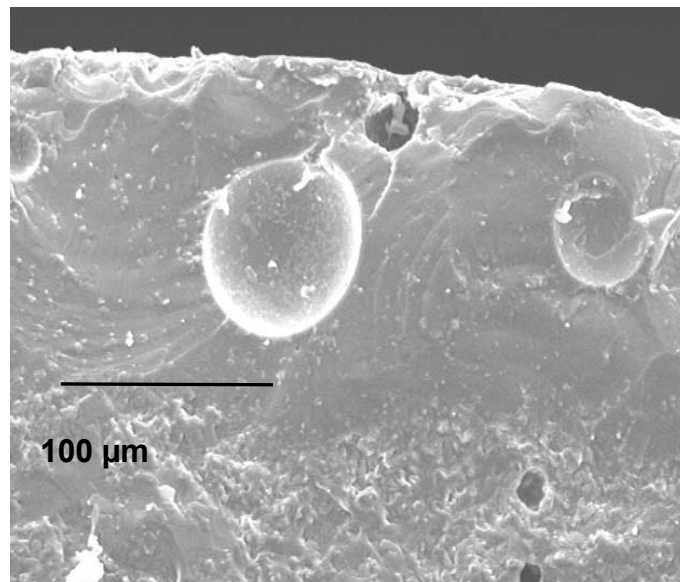


Figure 3.32. SEM micrograph of a bubble in the glaze as the strength-limiting flaw for alumina-body specimens with Glaze C, twice-dipped.

3.6.3 Weibull Analysis

Tables 3-IV and 3-V are a list of the type of fracture origin, location of fracture origin, and the relative size of the fracture origins, for the silica body and alumina body, respectively. This table shows that the lower-strength samples had larger

origins, usually bubbles that were generally located in the glaze. Flaw sizes were measured as the diameter of the flaw in the x-direction, i.e., left-right direction.

Table 3-IV. Fracture Origin Characterization for Silica-Body Samples

Glaze	Type of Flaw	Location of Flaw	Flaw Size (μm) (measured)
A	not identifiable	-	-
A2	samples crazed	-	-
B	bubbles	in glaze	80-100
B2	bubbles	in glaze	120-150
B (1350)	bubbles/inclusions	glaze/body	100-150
C	pores	interface	20-30
C2	bubbles	in glaze	60-80
D	grains	interface	40-50
D2	bubbles	in glaze	80-100
E	pores/microlamination	interface	80-100
E2	bubbles	in glaze	80-100
F	bubbles	interface	70-80
F2	bubbles	in glaze	80-100
Base	inclusions	body	70-80
Base2	grains/inclusions	body	60-80

*2 after the glaze indicates twice-dipped samples.

Table 3-V. Fracture Origin Characterization of Alumina-Body Samples

Glaze	Type of Flaw	Location of Flaw	Flaw Size (µm)
A	not identifiable	-	-
A2	crystals	on glaze surface	70-100
B	not identifiable	-	-
B2	bubbles	in glaze	90-100
B (1350)	large pores at the glaze/body interface due to surface layer on the body	-	-
C	pores	interface	20-30
C2	bubbles	in glaze	60-80
D	pores	interface	30-50
D2	crystals	on glaze surface	10-40
E	pores	interface	20-30
E2	grains	interface	30-40
F	pores	interface	30-40
F2	bubbles	in glaze	80-90
Base	grains/pores	body	20-40
Base2	grains/pores	body	20-40

*2 after the glaze indicated twice-dipped samples.

Weibull statistics indicate there was little scatter in the strength data for both sets of bodies. Weibull plots can be found in Figures 3.33-3.36, and a list of strength, Weibull modulus (m), and R^2 values are found in Tables 3-VI and 3-VII. Samples that were twice-dipped with Glazes A and D on the alumina body were exceptions in that these samples had much more scatter in the strength data. This is attributed to the fact that these samples had fracture origins that were crystals found on the glaze surface. These samples had a larger distribution of flaw sizes, verified by fractography, and, therefore, a larger amount of scatter in the data. The samples twice-dipped with Glaze A on the silica body crazed. These samples then had a broad distribution of flaw sizes.

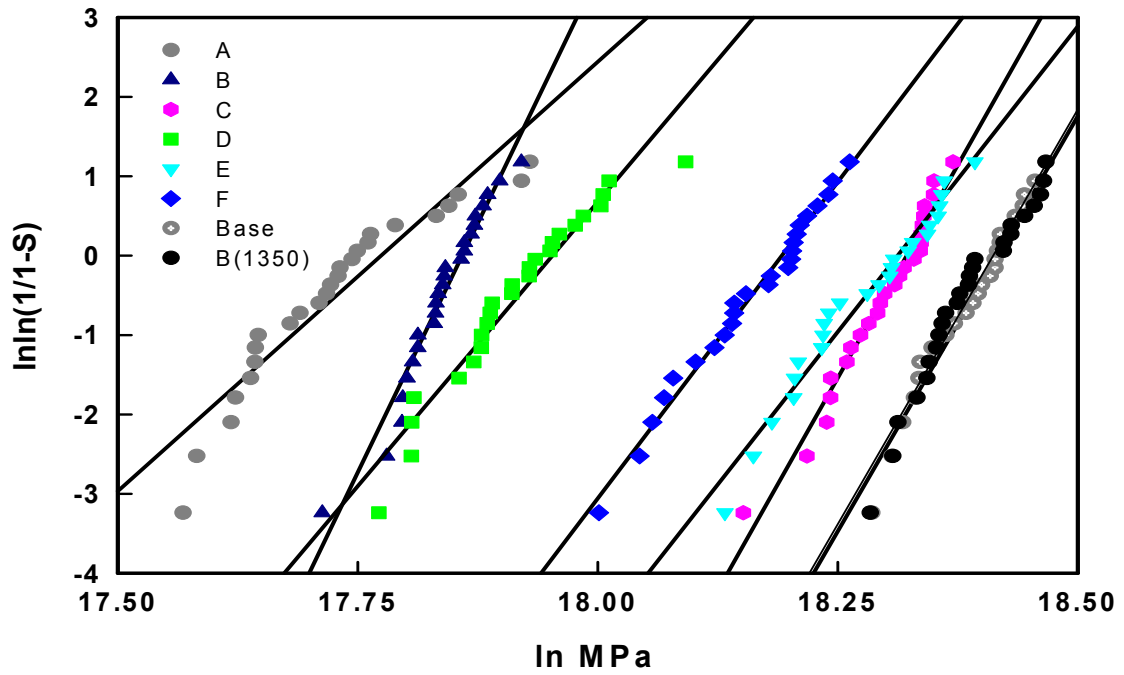


Figure 3.33. Weibull plot for the silica body, for the once-dipped samples.

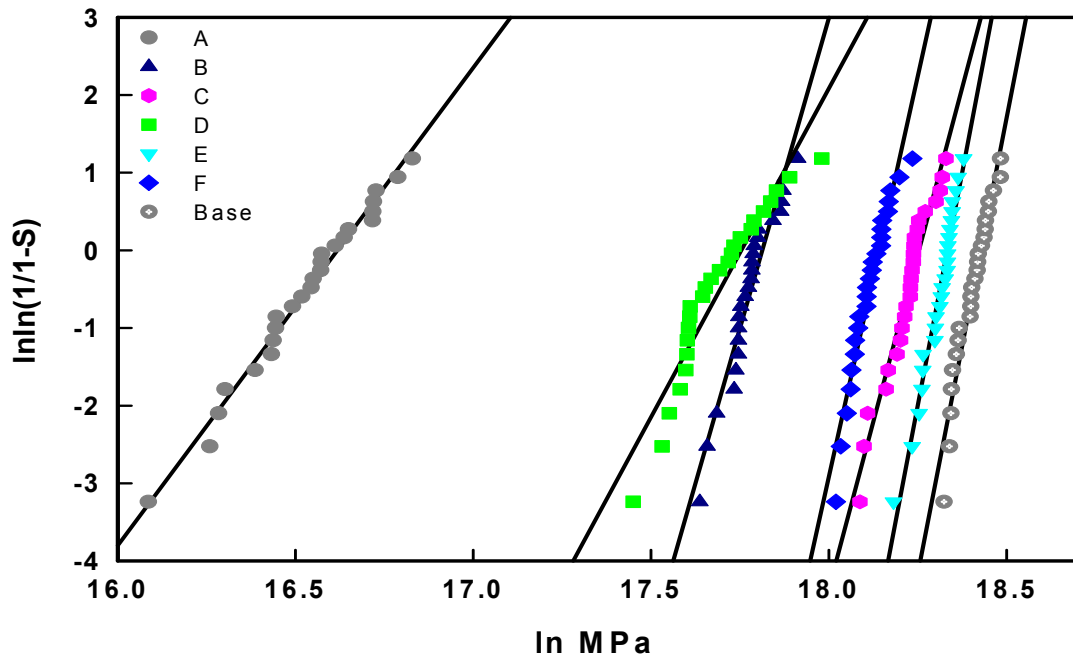


Figure 3.34. Weibull plot for the silica body, twice-dipped samples.

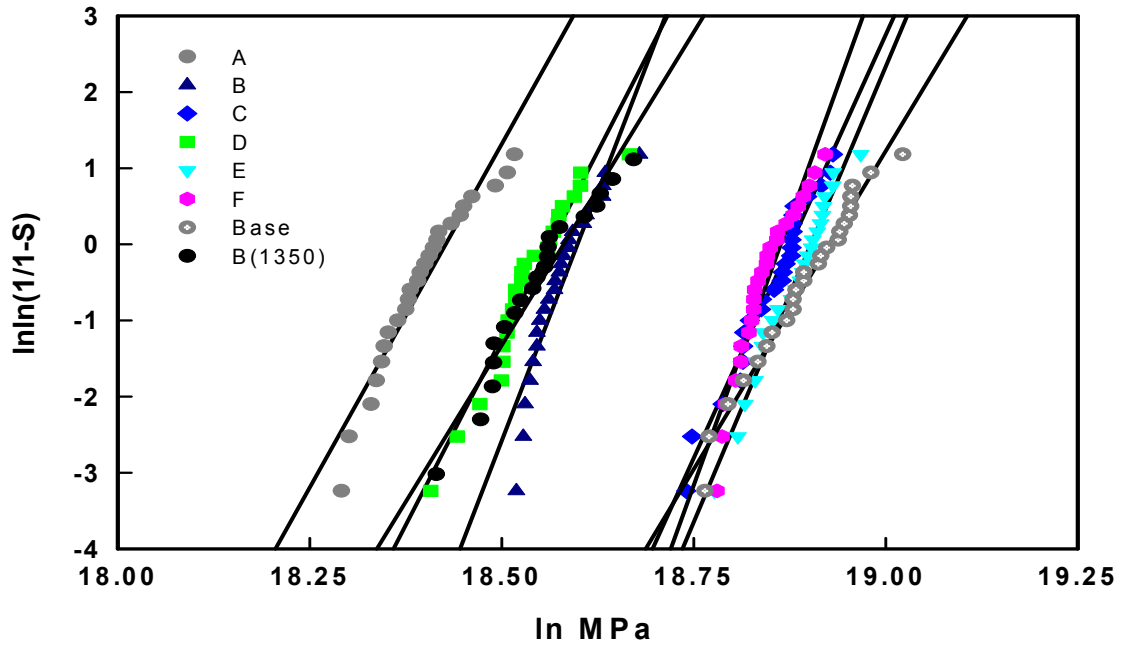


Figure 3.35. Weibull plot for the alumina body, once-dipped samples.

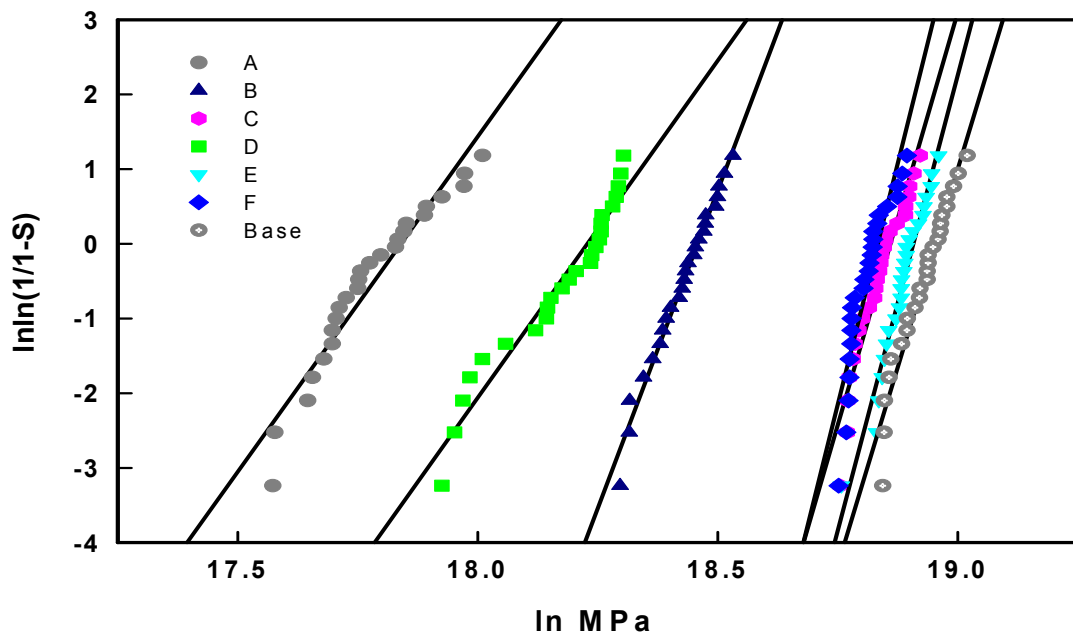


Figure 3.36. Weibull plot for the alumina body, twice-dipped samples.

Table 3-VI. σ , m , and R^2 Values for the Silica Body Samples

Glaze	Strength (MPa)	Weibull Modulus	R^2
A	50	11	0.90
A2	15	6	0.99
B	55	25	0.96
B2	52	16	0.93
B(1350)	97	21	0.96
C	88	21	0.97
C2	82	17	0.95
D	60	14	0.94
D2	48	8	0.91
E	86	15	0.97
E2	89	24	0.97
F	77	16	0.99
F2	73	21	0.94
Base	97	21	0.96
Base2	98	23	0.95

*2 after the glaze indicated twice-dipped samples.

Table 3-VII. σ , m , and R^2 Values for Alumina Body Samples

Glaze	Strength (MPa)	Weibull Modulus	R^2
A	97	18	0.93
A2	53	9	0.93
B	117	26	0.87
B2	100	17	0.98
B(1350)	114	16	0.94
C	154	22	0.97
C2	151	22	0.93
D	112	20	0.93
D2	78	9	0.95
E	158	24	0.98
E2	159	24	0.96
F	152	28	0.92
F2	148	26	0.85
Base	161	17	0.98
Base2	166	21	0.95

*2 after the glaze indicated twice-dipped samples.

3.7 Glaze/Body Interface

Observations were made in conjunction with the amount of reaction at the glaze/body interface and the strength of the sample. The high-strength samples had glaze/body interfaces that made it difficult to distinguish where the body ended and the glaze began, as seen in Figure 3.37. These samples had a large interfacial region. The base-glaze samples have the largest interfacial region. The low-strength samples had glaze/body interfaces that were distinct. It was obvious where the body ended and the glaze began, as seen in Figure 3.38.

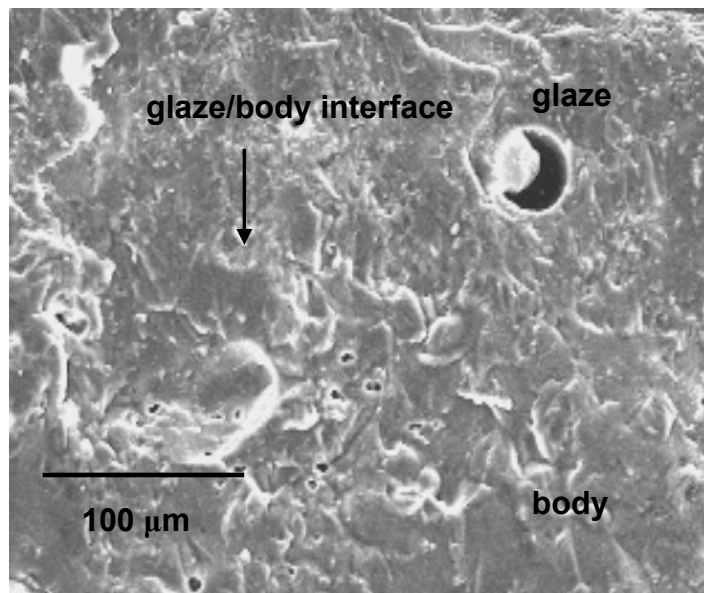


Figure 3.37. SEM micrograph of a high-strength sample, Base glaze on the silica body, with a nondistinct glaze/body interface.

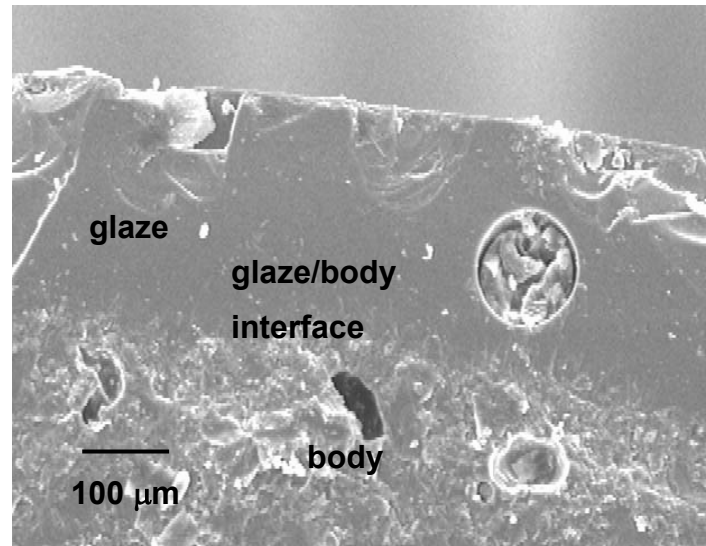


Figure 3.38. SEM micrograph of a low-strength sample, Glaze D on the alumina body, with a distinct glaze/body interface.

4 CONCLUSIONS

Through the use of flexure testing and fractographic analysis, the effect of multiple glaze variables on the mechanical strength of two commercial porcelain bodies was characterized. Glaze composition was systematically altered through varying the SiO₂ level in the glaze. This in turn, caused a change in the thermal expansion of the glaze. As the amount of thermal expansion mismatch between the glaze and the body was increased, the strength of the samples increased. For the silica body, it appears that a maximum value in strength, of 97 MPa, has been reached. Once the level of mismatch between the body and glaze reached $0.93 \times 10^{-6}/K$, further mismatch caused no statistically significant increase in strength. The alumina body reached a maximum in strength, of 161 MPa, when a mismatch between body and glaze reached a level of $1.13 \times 10^{-6}/K$.

It was shown that the strength of a piece can be predicted if two things are known: (1) the amount of thermal expansion mismatch between the body and glaze and (2) the Young's Modulus of the body. Both the alumina and silica bodies behaved similarly when the Young's Modulus of the respective body was taken into account. This was shown by both bodies having the same slope of the linear regression line that was fit to the data.

Undissolved quartz was present in Glaze B. The quartz caused an increase in the thermal expansion of the glaze. When the glaze was fired to a higher temperature and all of the quartz was dissolved, the thermal expansion of the glaze decreased. Therefore, it is not always true to say that increasing the amount of silica in a glaze will lower its thermal expansion. This is only true if there is no undissolved quartz present in the glaze.

Fractography analysis showed that the lowest-strength samples, for both glaze thicknesses, had fracture origins that were primarily located in the glaze. The

origins were determined to be bubbles present in the glaze. The medium-strength samples had fracture origins that were located at the glaze/body interface and were primarily pores. When the glaze thickness was increased, the fracture origins were then located in the glaze and were identified as bubbles. The highest-strength samples, for both glaze thicknesses, had fracture origins that were mostly located in the body, and were identified as pores and grains. The lower-strength samples had fracture origins that were much larger than the higher-strength samples.

5 FUTURE WORK

It is important to understand the affect of many glaze variables on the mechanical strength of a whiteware to produce strong and reliable products. It has been shown there is a possibility of predicting the strength of a whiteware for a any given Δ CTE value. Therefore, it would be useful to determine how thermal expansion mismatch affects the strength of several commercial porcelain bodies. If it is shown that these bodies show the same trend as the bodies that have been studied here it is suggested that a company will be able to predict the strength of their product at a given Δ CTE value.

REFERENCES

1. D. F. Funk, "Compressive Glaze Strengthening of High Strength Porcelain"; B.S. Thesis. Alfred University, Alfred, NY, 1978.
2. J. E. Funk, I. Knickerbocker, W. Curtis, D. Miller, and G. Steere, "Improvement of Mechanical and Electrical Strength of Porcelain," Electrical Power Research Institute, EL-721-SY, Res. Proj. 424-1, 1978.
3. S. Lampron, "Strength Differences in Glazed-Unglazed Ceramic Systems as a Result of Quartz Grain Impurities Existing at the Interface"; M.S. Thesis. Alfred University, Alfred, NY, 1983.
4. D. A. Duke, J. E. Megles, J. F. MacDowell, and H. F. Bopp, "Strengthening Glass-Ceramics by Application of Compressive Glazes," *J. Am. Ceram. Soc.*, **51** [2] 98-102 (1968).
5. L. E. Thiess, "Influence of Glaze Composition on the Mechanical Strength of Electrical Porcelain," *J. Am. Ceram. Soc.*, **19** [3] 70-3 (1936).
6. W. C. Bell and J. H. Koenig, "Effect of Glaze Film on Properties of a Vitreous China Body," *J. Am. Ceram. Soc.*, **24** [11] 341-8 (1941).
7. A. B. Feinberg, "The Effect of Glaze Stress on Mechanical Strength of Electrical Porcelains"; M.S. Thesis. Alfred University, Alfred, NY, 1985.
8. E. Gerold, "Influence of the Glaze upon the Physical Properties of Porcelain," *Hermsdorf-Schomburg Mitt.*, **15**, 395-497 (1925).
9. B. Pinto, "The Effect of Quartz Particle Size on Porcelain Strength"; M.S. Thesis. Alfred University, Alfred, NY, 2001.
10. W. M. Carty, Alfred University, Alfred, NY, March, 2003, Private Communication.
11. C. Radford, "A New Instrument for Assessing Body/Glaze Fit," *Br. Ceram. Trans. J.*, **76** [3] xx-xxv (1977).
12. A. A. Griffith, *Phil. Trans. R. Soc.*, **A221**, 163 (1920). As cited in W. D. Kingery, H. K. Bowen, and D. R. Uhlman, *Introduction to Ceramics*, 2nd ed. John Wiley & Sons, New York, 1960.
13. W. D. Kingery, H. K. Bowen, and D. R. Uhlmann, *Introduction to Ceramics*, 2nd ed. John Wiley & Sons, New York, 1960.

14. W. C. Bell, "A Study of Glaze Stresses," *Bull.-Ohio State Univ., Eng. Exp. Stn.*, **XII** [1] 19-25 (1943).
15. V. D. Frechette and T. A. Michalske, "Glaze-Stress Calculation from Ring-Test Data," *J. Am. Ceram. Soc.*, **63** [11-12] 712-3 (1980).
16. A. P. Cronin and M. J. Reece, "Thermal Stresses in Glazed Substrates," pp. 411-8 Joinings and Coatings, in *4th European Ceramic Society Conference Proceedings*. Vol. 9. Edited by B. S. Tranching and A. Bellosi. Gruppo Editoriale Faenza Editrice, Florence, Italy, 1995.
17. C. W. Parmelee, *Ceramic Glazes*. Industrial Publications, Chicago, 1948.
18. C. W. Parmelee, *Ceramic Glazes*, 3rd ed. Cahners Book, Boston, MA, 1973.
19. E. Thomas, M. A. Tuttle, and E. Miller, "Study of Glaze Penetration and Its Effect on Glaze Fit: I-III," *J. Am. Ceram. Soc.*, **28** [2] 52-4 (1945).
20. J. M. Cerdan and W. C. LaCourse, "Studies of Interfacial Reactions in Glaze-Body Systems," pp. 233-51 in *Technical Innovations in Whitewares*. Edited by J. S. Reed, J. E. Funk, P. F. Johnson, and J. R. Varner. Alfred University Press, Alfred, NY, 1981.
21. J. R. Varner and V. D. Frechette, "Fractography of Whitewares," pp. 305-15 in *Science of Whitewares*. Edited by V. E. Henkes, G. Y. Onoda, and W. M. Carty. American Ceramic Society, Westerville, OH, 1996.
22. J. J. Swab, M. J. Slavin, and G. D. Quinn, "Fracture Origins in Advanced Structural Ceramics," *Am. Ceram. Soc. Bull.*, **71** [11] 1639-40 (1992).
23. V. D. Frechette, *Failure Analysis of Brittle Materials*; pp. 14-31. American Ceramic Society, Westerville, OH, 1990.
24. R. Danzer and T. Lube, "R-Curve Behavior, Toughness Determination and Thermal Shock," pp. 425-39 in *Fracture Mechanics of Ceramics*, Vol. 11. Edited by R. C. Bradt. Plenum Press, New York, 1996.
25. G. D. Quinn, "Fractography and Estimates of Fracture Origin Size from Fracture Mechanics," *Ceram. Eng. Sci. Proc.*, **17** [3] 51-8 (1996).
26. D. A. Krohn and D. P. H. Hasselman, "Relation of Flaw Size to Mirror in the Fracture of Glass," *J. Am. Ceram. Soc.*, **54** [8] 411 (1971).

27. J. J. Mecholsky, S. W. Freiman, and R. W. Rice, "Fracture Surface Analysis of Ceramics," *J. Mater. Sci.*, **11** [7] 1310-9 (1976).
28. J. J. Mecholsky, R. W. Rice, and S. W. Freiman, "Prediction of Fracture Energy and Flaw Size in Glasses from Measurements of Mirror Size," *J. Am. Ceram. Soc.*, **57** [10] 440-3 (1974).
29. K. R. McKinney, "Relation of Fracture Mechanics to Mirror Surfaces of Fractured Brittle Materials," *J. Am. Ceram. Soc.*, **56** [4] 225 (1973).
30. G. D. Quinn, "Design Data for Engineering Ceramics: A Review of the Flexure Test," *J. Am. Ceram. Soc.*, **74** [9] 2037-66 (1991).
31. H. Peterlik, "Relationship of Strength and Defects of Ceramic Materials and Their Treatment by Weibull Theory," *J. Ceram. Soc. Jpn.*, **109** [8] S121-S6 (2001).
32. H. Dannheim, H. J. Oel, and P. Rivera, "Effect of Production Parameters on the Variation of Industrial Porcelain Strength Values," *Ceram. Forum Int.*, **68** [3] 66-71 (1991).
33. D. Doshi and J. S. Reed, "Critical Flaws in Sintered Compacts of Alumina Granules," *Ceram. Eng. Sci. Proc.*, **16** [5] 939-48 (1995).
34. H. A. Seger, *The Collected Writings of Hermann August Seger*, 1st ed.; pp. 230-49. Chemical Publishing, Easton, PA, 1902.
35. M. Paganelli, "Optical Non-Contact Dilatometry," *Ceram. World Rev.*, **10** [38] 234-9 (2000).
36. "Standard Test Method for Flexural Strength of Advanced Ceramics at Ambient Temperature," ASTM Standard C1161-94. American Society for Testing and Materials, West Conshohocken, PA.
37. G. D. Quinn, L. Ives, S. Jahanmir, and P. Koshy, "Fractographic Analysis of Machining Cracks in Silicon Nitride Rods and Bars," pp. 343-65 in *Ceramic Transactions*, Vol. 122. Edited by J. R. Varner, V. D. Frechette, and G. D. Quinn. American Ceramic Society, Westerville, OH, 2001.
38. "Standard Test Methods for Apparent Porosity, Water Absorption, Apparent Specific Gravity, and Bulk Density of Burned Refractory Brick and Shapes by Boiling Water," ASTM Standard C 20-87. American Society for Testing and Materials, West Conshohocken, PA.

39. "Standard Test Method for Density of Glass by Bouyancy," ASTM Standard C 693-93. American Society for Testing and Materials, West Conshohocken, PA.
40. R. Jenkins and R. L. Snyder, *Introduction to X-Ray Powder Diffractometry*; p. 153. John Wiley and Sons, New York, 1996.
41. D. Seymour, "Phase Evolutions in Electrical Porcelains during Firing"; M. S. Thesis. Alfred University, Alfred, NY, 2000.
42. A. K. Varshneya, *Fundamentals of Inorganic Glasses*; pp. 254-64. Academic Press, San Diego, CA, 1994.
43. D. Earl, Alfred University, Alfred, NY, December, 2002, Private Communication.
44. A. M. Blakely, "Life History of a Glaze: II, Measurement of Stress in a Cooling Glaze," *J. Am. Ceram. Soc.*, **28** [7] 243-51 (1938).

APPENDIX A

Table A-I. Raw Materials Suppliers for Glazes (A, B, C, D, E, and F)

Raw Material	Supplier	Location
G-200	The Feldspar Corp.	Atlanta, GA
EPK	The Feldspar Corp.	Atlanta, GA
Ceramtaic I	R.T. Vanderbilt Company, Inc.	Norwalk, CT
Whiting	Snowcal	London, England
Flint	Oglebay Norton	Glenford, OH
Soda Ash	General Chemica	Parsipanny, NJ
Pearl Ash	Armand Products Co.	Princeton, NJ

Table A-II. Chemical Analysis of Glazes and Bodies

Oxide (wt%)	Sample								
	Glaze A	Glaze B	Glaze C	Glaze D	Glaze E	Glaze F	Base Glaze	Silica Body	Alumina Body
SiO ₂	65.39	74.21	62.32	62.41	65.78	69.58	63.40	62.18	41.08
Al ₂ O ₃	14.00	10.84	12.44	13.96	11.21	11.02	10.50	25.13	47.96
Fe ₂ O ₃	0.24	0.19	0.32	0.27	0.30	0.23	0.38	0.51	0.48
MgO	3.01	2.34	2.41	2.83	2.10	2.22	1.96	0.15	0.14
CaO	8.71	5.65	9.11	9.47	8.23	7.49	8.33	0.35	0.31
Na ₂ O	1.56	1.24	1.10	1.47	0.92	1.13	0.53	1.03	1.00
K ₂ O	6.35	4.94	4.21	5.52	3.41	4.22	2.01	3.79	3.46
TiO ₂	0.07	0.07	0.28	0.16	0.28	0.16	0.37	0.65	0.58
Sr (ppm)	245	174	10054	4639	10633	4780	15382	140	131
Zr (ppm)	43	44	42058	19267	43103	19754	69356	136	104

APPENDIX B

UMF sample calculation using the chemical analysis of the Base glaze, listed in Appendix A.³⁴

1) Convert each oxide wt% to mole %. Assume there are 100 g so the wt% is equal to the number of grams. Divide the molecular weight each oxide by the number of grams of the oxide to obtain the number of moles of each oxide.

Oxide	Wt%	MW (g/mole)	moles
Na ₂ O	0.53	62.00	0.009
K ₂ O	2.01	94.20	0.021
MgO	1.96	40.32	0.049
CaO	8.33	56.08	0.149
SrO	1.82	103.63	0.018
Al ₂ O ₃	10.50	101.96	0.103
SiO ₂	63.40	60.09	1.055
ZrO ₂	9.37	123.22	0.076

2) Add the moles of fluxes together (R₂O + RO oxides)

$$0.009 + 0.021 + 0.049 + 0.149 + 0.018 = 0.245 \text{ moles}$$

3) Divide each oxide by the flux total from the previous step to normalize the batch to the fluxing oxides.

Oxide	moles		Flux Total		Normalized Ratio
Na₂O	0.009	÷	0.245	=	0.03
K₂O	0.021	÷	0.245	=	0.09
MgO	0.049	÷	0.245	=	0.20
CaO	0.149	÷	0.245	=	0.61
SrO	0.018	÷	0.245	=	0.07
Al₂O₃	0.103	÷	0.245	=	0.42
SiO₂	1.055	÷	0.245	=	4.31
ZrO₂	0.076	÷	0.245	=	0.31

APPENDIX C

Calculation of Poisson's Ratio (μ) and Young's Modulus (E) using the pulse echo technique.

Calculation of the velocity of sound in the transverse and longitudinal directions

$$V(\text{m/s}) = \frac{\text{thickness}}{0.5 \text{round-trip transittime}} \quad (\text{C-1})$$

Calculation of Poisson's Ratio

$$\mu = \frac{1 - 2(V_T / V_L)^2}{2 - 2(V_T / V_L)^2} \quad (\text{C-2})$$

where:

V_T =transverse velocity

V_L =longitudinal velocity

Calculation of Young's Modulus

$$E(\text{GPa}) = V_L^2 \rho \frac{(1 + \mu)(1 - 2\mu)}{1 - \mu} \quad (\text{C-3})$$

where:

ρ =density (kg/m^3)

APPENDIX D

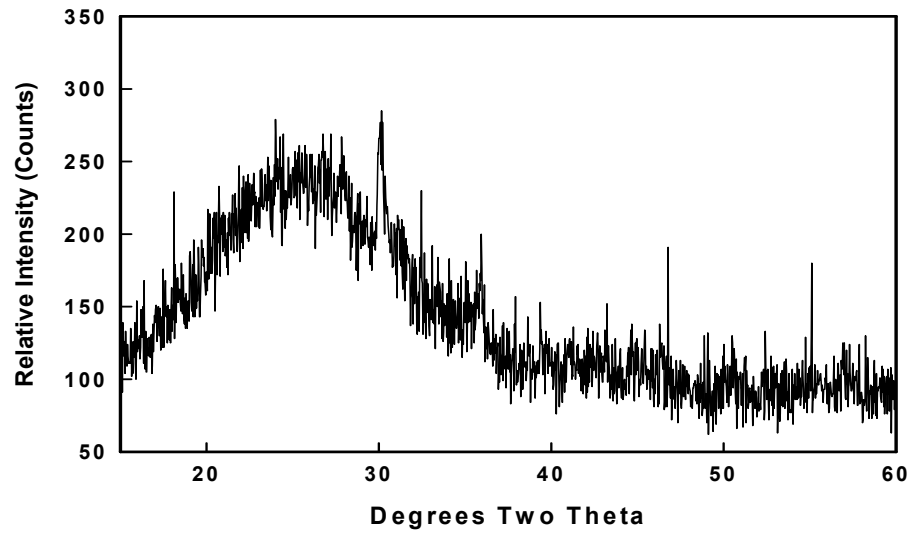


Figure D.1. XRD pattern for Glaze A. No crystallizing species are present.

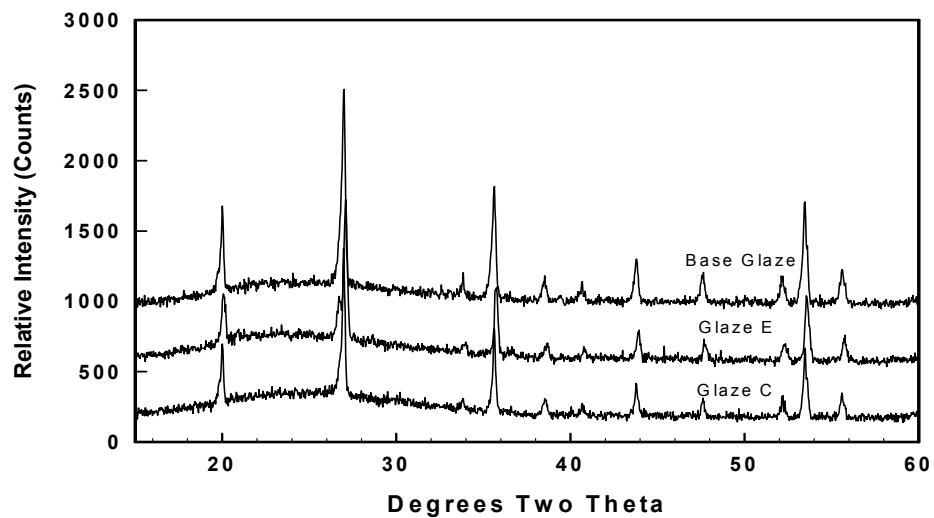


Figure D.2. XRD patterns for Glazes C, E and the Base glaze with zircon being the crystalline species.

Appendix E

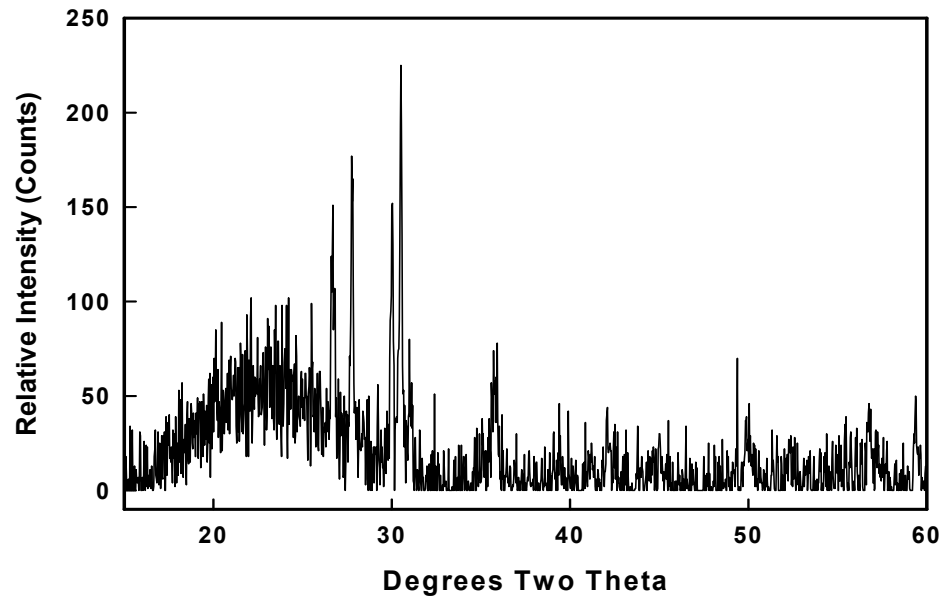


Figure E.1. XRD pattern of Glaze A, twice-dipped, on the alumina body. The crystalline species is diopside ($\text{CaO}\cdot\text{MgO}\cdot 2\text{SiO}_2$).

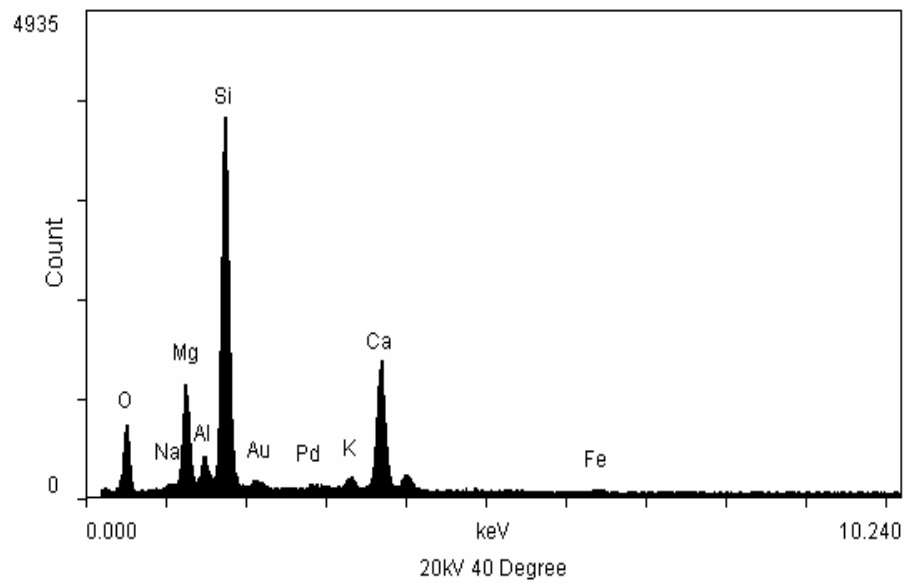


Figure E.2. EDS pattern of Glaze A, twice-dipped, on the alumina body, confirming that diopside was the crystalline species.